# *Colloquium*: Heavy-electron quantum criticality and single-particle spectroscopy

Stefan Kirchner*

*Zhejiang Institute of Modern Physics, Zhejiang University, Hangzhou, Zhejiang 310058, China and Zhejiang Province Key Laboratory of Quantum Technology and Device, Zhejiang University, Hangzhou 310027, China*

Silke Paschen

*Institute of Solid State Physics, Vienna University of Technology, Wiedner Hauptstrasse 8-10, 1040 Vienna, Austria*

Qiuyun Chen

*Science and Technology on Surface Physics and Chemistry Laboratory, Mianyang 621908, China*

Steffen Wirth

*Max Planck Institute for Chemical Physics of Solids, 01187 Dresden, Germany*

Donglai Feng

*State Key Laboratory of Surface Physics, and Department of Physics, Fudan University, Shanghai 200433, China and Hefei National Laboratory for Physical Science at Microscale, CAS Center for Excellence in Quantum Information and Quantum Physics, and Department of Physics, University of Science and Technology of China, Hefei 230026, China*

Joe D. Thompson

*Los Alamos National Laboratory, Los Alamos, New Mexico 87545, USA*

Qimiao Si

*Department of Physics and Astronomy and Center for Quantum Materials, Rice University, Houston, Texas 77005, USA*

(published 9 March 2020)

Angle-resolved photoemission spectroscopy (ARPES) and scanning tunneling microscopy (STM) have become indispensable tools in the study of correlated quantum materials. Both probe complementary aspects of the single-particle excitation spectrum. Taken together, ARPES and STM have the potential to explore properties of the electronic Green's function, a central object of many-body theory. This review explicates this potential with a focus on heavy-electron quantum criticality, especially the role of Kondo destruction. A discussion on how to probe the Kondo destruction effect across the quantum-critical point using ARPES and STM measurements is presented. Particular emphasis is placed on the question of how to distinguish between the signatures of the initial onset of hybridization-gap formation, which is the "high-energy" physics to be expected in all heavy-electron systems, and those of Kondo destruction, which characterizes the low-energy physics and, hence, the nature of quantum criticality. Recent progress and possible challenges in the experimental investigations are surveyed, the STM and ARPES spectra for several quantum-critical heavy-electron compounds are compared, and the prospects for further advances are outlined.

DOI: 10.1103/RevModPhys.92.011002

*stefan.kirchner@correlated-matter.com

 

## CONTENTS



## I. INTRODUCTION

A major objective of quantum materials research is to link observable properties to the nature of quantum mechanical many-body ground state properties and to the characteristics of the excitation spectrum above the ground state. In particular, it aims at understanding and predicting the emergence of novel phases in terms of a minimal set of variables, most notably symmetries and broken symmetries of the ground state and the ensuing classification of the excitation spectrum. The typical energy window commonly involved in the materials of interest can cover a wide range, from a few percent of a meV to several eV. A well-known example is the high-temperature superconductors, which have stimulated research since their discovery more than 30 years ago.

The quest for a unified understanding of different classes of quantum materials has led to the notion of quantum-critical points (QCPs) as an economic and powerful way of organizing their phase diagrams (Sachdev, 1999; Coleman and Schofield, 2005; Si and Steglich, 2010; Kirchner, Stockert, and Wirth, 2013). Such continuous zero-temperature phase transitions not only separate different ground states but also give rise to a characteristic behavior; this is the quantum-critical fan, which can extend to comparatively large energies and temperatures, cf. Fig. 1. Within this fan, universal scaling behavior is expected up to some material-specific high-energy cutoff. Among the material classes that are currently attracting particular interest are the cuprates, iron pnictides, pyrochlore iridates, transition metal dichalcogenides, and heavy-electron compounds. An underlying theme of most if not all of these materials classes is the tendency of their charge carriers to localize in response to the large effective Coulomb repulsion experienced by the itinerant degrees of freedom. The tendency toward localization gives rise to the bad-metal behavior of these materials.

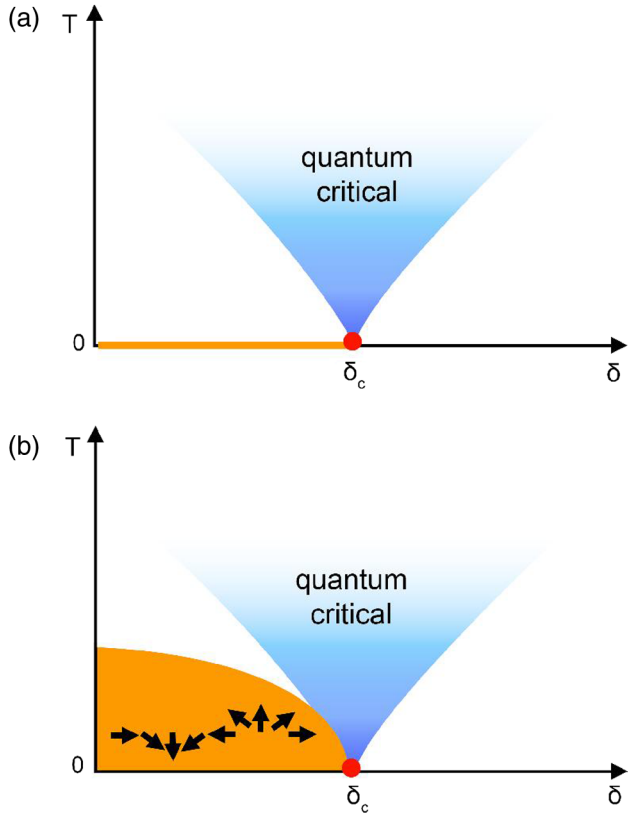


FIG. 1. The quantum-critical fan. (a) A continuous quantum phase transition occurs at zero temperature for a critical value ($\delta_c$) of a nonthermal tuning parameter $\delta$. It separates the distinct behaviors of the ground state wave function, i.e., being ordered for $\delta < \delta_c$ (orange line) and disordered for $\delta > \delta_c$. At nonzero temperatures vestiges of the quantum phase transition lead to distinctive scaling behavior in a quantum-critical fan that spreads out of the quantum-critical point and extends up to a problem specific cutoff temperature. Unlike the scaling behavior, the existence of a fan of quantum-critical behavior is generic, independent of the nature of the criticality. (b) Frequently, quantum phase transitions occur as order is suppressed and the transition temperature $T_c(\delta)$ of a classical phase transition vanishes, i.e., $T_c(\delta \to \delta_c) \to 0$. In heavy-electron materials, the most common types of quantum criticality separate antiferromagnetic and paramagnetic phases. Shown here is a type of antiferromagnetic order, indicated by the variation of the magnetic moment density over one wavelength. This Colloquium explores the potential of single-particle spectroscopies to distinguish different types of quantum criticality.

In heavy-electron compounds, which most commonly are based on Ce, Yb, and U, the primary degree of freedom is the $f$ electron. In the lanthanide-based materials, the $4f$ electron is localized close to the ionic core as a result of atomic physics and thus has a characteristic energy of the order of eV. For the same reason, the wave-function overlap between the $4f$ orbitals and the band (or $c$) electrons, i.e., the hybridization, is typically small. As a result, the $4f$ electron appears localized at high temperatures or energies in the entire range

of phase space as long as the valency of the lanthanide ion remains near its localized limit. In this regime each $4f$ electron contributes an amount $\sim \ln N_f$ to the entropy, where $N_f$ is the angular momentum degeneracy. $N_f$ is affected by spin-orbit coupling and the crystal electric fields but as long as $N_f > 1$, the spin entropy remains macroscopically large.

Similar arguments in principle apply to actinide-based heavy-electron compounds (Fisk *et al.*, 1985). In contrast to their $4f$ counterparts, $5f$ orbitals are substantially less localized. As a result, the associated heavy-electron bands are more dispersive, $f-c$ hybridization is stronger and crystal electric fields are less well defined. Collectively, these properties frequently lead to more complex behaviors compared to Ce- or Yb-based intermetallics (Lawrence *et al.*, 2011), and so we use the lanthanide-based heavy-electron materials as exemplary of the essential physics. As temperature is lowered and the ground state is approached, the spin entropy associated with the localized $4f$ ($5f$) electron needs to be quenched. Evidently, the system possesses several options for releasing this entropy, which lead to different ground states. At zero temperature, the system can transition from one ground state to another upon changing coupling constants in the Hamiltonian. At values of these coupling constants where the ground state energy is nonanalytic, the system undergoes a quantum phase transition. Experiments, however, are performed at nonzero temperatures. The challenge then is how to distinguish the approach to different ground states with only a limited, intermediate temperature window accessible to experiment. This task is made even more difficult given that high-energy properties are largely insensitive to the changes in the coupling constants that take a system through different ground states.

The primary tools for exposing the underlying physics that accompanies the entropy release as the temperature or energy is lowered include spectroscopic methods that can trace excitations over some energy range of interest. For example, spin excitations can be probed with the help of inelastic neutron scattering. Among the various spectroscopic techniques, angle-resolved photoemission spectroscopy (ARPES) and scanning tunneling microscopy or spectroscopy (STM) stand out as these allow one to most directly trace properties of the single-particle Green's function, the basic building block in almost every many-body theory.

We survey and compare recent ARPES and STM experiments performed on quantum-critical heavy-electron compounds that are located close to ground state instabilites at the border of magnetism. In particular, we focus on how critical Kondo destruction (Coleman *et al.*, 2001; Si *et al.*, 2001), i.e., the breakdown of Kondo entanglement at zero temperature right at the onset of magnetism, is reflected in ARPES and STM data at elevated temperatures.

This Colloquium is organized as follows. After a brief introduction of quantum criticality in heavy-electron systems, we recapitulate the relation between APRES and STM measurements and their link with the single-particle Green's function. We then discuss recent STM measurements on $YbRh_2Si_2$, a heavy-electron antiferromagnet that features a Kondo destruction QCP as a function of the applied magnetic field, before turning to high-resolution ARPES measurements on the cerium-115 family that consists of $CeMIn_5$ ($M$ = Co, Rh, Ir). We close with an outlook on current challenges and future directions. To facilitate reading, each section (II–V) ends with a brief summary of the salient points discussed in the section.

## II. QUANTUM CRITICALITY

Quantum phase transitions occur at zero temperature and like their finite temperature counterparts, they can be either first order or continuous (Sachdev, 1999; Löhneysen *et al.*, 2007; Gegenwart, Si, and Steglich, 2008; Si and Steglich, 2010). In contrast to the finite temperature case where thermal fluctuations drive the transition, quantum fluctuations, encoded already at the Hamiltonian level, are responsible for the occurrence of a quantum phase transition. A classical transition can be accessed by varying the temperature through a threshold value $T_c$, while the zero-temperature transition is approached by tuning a nonthermal control parameter, denoted $\delta$ in Fig. 1, to its critical value ($\delta_c$). If the transition is continuous, characteristic, critical scaling ensues in its vicinity which reflects the singular correlations of the ground state wave function at $\delta_c$. At nonzero temperatures, this singular behavior leads to the quantum-critical fan in which characteristic behavior is observed in various quantities below a system-specific cutoff energy; see Fig. 1.

In stoichiometric heavy-electron compounds containing Ce or Yb elements, $4f$ electrons in a partially filled $4f$ shell are strongly correlated, provided the Ce or Yb ions possess a valence close to +III. The spin-orbit interaction and the crystal electric field generated by the ligands surrounding the Ce or Yb ion in the crystalline environment reduce the degeneracy of the $4f$ shell. Most commonly, the lowest lying atomic $4f$ levels correspond to a Kramers doublet. As a result, the $4f$ electrons behave as a lattice of effective spin-1/2 local moments. This leads to an effective description in terms of the Kondo lattice Hamiltonian:

$$H_{\mathrm{KL}} = H_0 + \sum_{ij} I_{ij}\mathbf{S}_i \cdot \mathbf{S}_j + \sum_i J_K \mathbf{S}_i \cdot \mathbf{s}_i^c, \qquad (1)$$

where $H_0 = \sum_{\mathbf{k},\sigma} \varepsilon_{\mathbf{k}} c^\dagger_{\mathbf{k}\sigma} c_{\mathbf{k}\sigma}$ describes the conduction electrons with dispersion $\epsilon_{\mathbf{k}}$. The Ruderman-Kittel-Kasuya-Yosida (RKKY) interaction $I_{ij}$ between the local moments $\mathbf{S}$ at site $i$ and $j$ and the Kondo coupling $J_K$ (acting between the local moments and the conduction electron spin density $\mathbf{s}^c$) typically are antiferromagnetic, i.e., $I_{ij} > 0$, $J_K > 0$. The competition between these two types of interactions lies at the heart of the microscopic physics for heavy-electron systems (Doniach, 1977).

In the heavy-electron compounds described by the Kondo lattice Hamiltonian, Eq. (1), a QCP may arise from tuning the ratio of RKKY to Kondo interactions, which is parametrized by the nonthermal control paramater $\delta \equiv T_K^0/I$. Here the Kondo scale (for the $N_f = 2$ case) is $T_K^0 \approx \rho_0^{-1} \exp(-1/\rho_0 J_K)$, with $\rho_0$ being the density of states of the conduction electrons at the Fermi energy, whereas $I$ parametrizes the RKKY interaction. This RKKY exchange interaction between the localized moments is mediated by the conduction electron spin density. It is perturbatively generated from the Kondo coupling term $\sim J_K$, resulting in $I_{ij}(J_K)$. In

Eq. (1), we added $I_{ij}$ as an independent exchange interaction to facilitate the discussion of the phase diagram, because tuning the ratio between the explicit $I_{ij}$ and $J_K$ is more convenient. It accesses the quantum phase transition that otherwise would have been induced in the tuning of $\delta$ through the variation of the ratio of $J_K$ to the conduction electron bandwidth $2D \sim 1/\rho_0$. Formally, one may think of Eq. (1) as arising from a more complete starting Hamiltonian through the process of integrating out additional conduction electron degrees of freedom; this procedure results in the explicit $I_{ij}$ term in the effective Hamiltonian of Eq. (1). One needs to be sure that there is no double counting of the explicit and generated contributions to $I_{ij}$, and this can be consistently done in practice. For a technical discussion of this point see Si, Zhu, and Grempel (2005).

On the paramagnetic side, the ground state is characterized by the amplitude of the static Kondo singlets that are formed between the local moments and conduction electron spins (Hewson, 1993). For a Kondo destruction QCP, this static Kondo singlet amplitude is continuously suppressed when the system approaches the QCP from the paramagnetic side (Si *et al.*, 2001, 2014; Zhu, Grempel, and Si, 2003).

As illustrated in Fig. 2(a), the Kondo destruction energy scale $E^*_{\rm loc}$ goes to zero as the control parameter $\delta$ approaches the QCP at $\delta_c$ from the paramagnetic side, and the antiferromagnetic order sets in when $\delta$ goes across $\delta_c$. The Kondo destruction goes beyond the Landau framework of quantum criticality. The latter is based on order-parameter fluctuations, which in the present context of antiferromagnetic heavy-electron systems is referred to as a spin-density-wave (SDW) QCP (Hertz, 1976; Moriya, 1985; Millis, 1993). It arises when $E^*_{\rm loc}$ stays nonzero when decreasing $\delta$ to $\delta_c$ and approaches zero only inside the ordered regime at $\delta < \delta_c$. In this case, the asymptotic quantum-critical behavior at energies below $E^*_{\rm loc}(\delta_c)$ is the same as in the type of phase diagram shown in Fig. 1(b), where $E^*_{\rm loc}$ is not part of the critical physics.

The Kondo destruction gives rise to a dynamical spin susceptibility which displays unusual scaling at the QCP (Si *et al.*, 2001, 2014). This includes a fractional exponent (Grempel and Si, 2003; Zhu, Grempel, and Si, 2003; Glossop and Ingersent, 2007; Zhu *et al.*, 2007) in the singular dependence on frequency ($\omega$) and temperature ($T$), and $\omega/T$ scaling. These features have in fact been observed by inelastic neutron scattering measurements on the $5f$ electron system $UCu_{5-x}Pd_x$ (Aronson *et al.*, 1995) and the $4f$ electron-based metal $CeCu_{6-x}Au_x$ (Schröder *et al.*, 2000).

For $CeCu_{6-x}Au_x$ at its critical doping $x_c \approx 0.1$, the exponent in the $\omega/T$ scaling analysis (Schröder *et al.*, 2000) was found to be $\alpha = 0.75(5)$, which compares well with the value $\alpha = 0.72$–$0.78$ calculated at the Kondo destruction QCP (Grempel and Si, 2003; Zhu, Grempel, and Si, 2003; Glossop and Ingersent, 2007; Zhu *et al.*, 2007). In the case of a standard SDW QCP, no such $\omega/T$ scaling is expected as this QCP is described by a Ginzburg-Landau functional above its upper critical dimension (Hertz, 1976; Moriya, 1985; Millis, 1993).

In the single-particle excitations, the collapse of $E^*_{\rm loc}$ implies a sudden reconstruction of the Fermi surface across the QCP. To contrast this picture with the more traditional scenario of an SDW transition (Hertz, 1976; Moriya, 1985; Millis, 1993), where critical fluctuations are tied to nesting

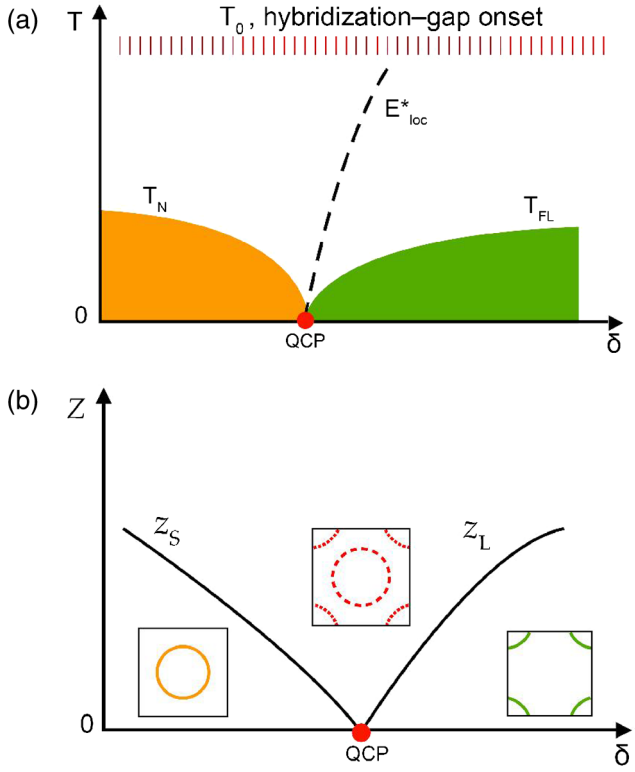


FIG. 2. Basic concepts of Kondo destruction quantum criticality. (a) Local quantum criticality with Kondo destruction under the variation of the control parameter $\delta$. Here $T_0$ is a high-energy scale that describes the initial onset of dynamical Kondo correlations and that smoothly evolves across the QCP $\delta_c$. This high-energy scale is reflected in the onset of hybridization-gap formation. The low-energy physics is described in terms of $T_N$ and $T_{\rm FL}$, which are, respectively, the temperatures for the Néel transition and the crossover into the paramagnetic Fermi liquid state. This phase diagram also involves the Kondo destruction energy scale $E^*_{\rm loc}$, which characterizes the Kondo destruction. The $E^*_{\rm loc}$ line divides the phase diagram in terms of the flow of the system toward either the Kondo screened or the Kondo destruction ground state. In the conventional model of spin-density-wave quantum criticality, the line $E^*_{\rm loc}$ extrapolates to zero temperature in the ordered phase so that the Fermi surface already is large before reaching the QCP with increasing $\delta$ and evolves smoothly across the QCP (Coleman *et al.*, 2001; Si *et al.*, 2001). Adapted from Stockert *et al.*, 2012. (b) The small (left) and large (right) Fermi surfaces and the associated quasiparticle weights $z_S$ and $z_L$ that are discussed in Sec. III. The fluctuating Fermi surfaces (middle) are associated with the QCP. Adapted from Pfau *et al.*, 2012.

properties of the Fermi surface, we refer to quantum criticality exhibiting critical Kondo destruction as local quantum criticality (Coleman *et al.*, 2001; Si *et al.*, 2001; Senthil, Vojta, and Sachdev, 2004; Pépin, 2007). At zero temperature:

- For $\delta > \delta_c$, the Fermi surface is large and is given by the combination of the $4f$ and conduction electrons. A nonzero amplitude of the static Kondo singlet specifies a Kondo screened ground state. Here, Kondo resonances appear in the excitation spectrum, reflecting the entanglement between the $4f$ moments and the conduction electrons in the ground state. The Kondo effect is

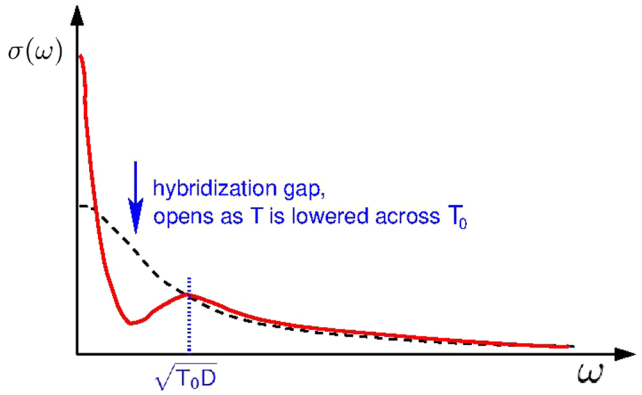


FIG. 3. Sketch of the optical conductivity $\sigma(\omega)$ for temperatures well above (dashed black line) and well below (continuous red line) the crossover temperature scale $T_0$. Here the lowering of temperature through $T_0$ is accompanied by the onset of the hybridization gap. The characteristic frequency scale for the hybridization gap is $\sqrt{T_0 D}$ (the vertical dotted blue line), where $D$ is an energy scale of the order of the conduction electron bandwidth. At low energies, i.e., for $\omega \ll T_0$ and $T \ll T_0$, and sufficiently far away from quantum criticality (i.e. $\delta < \delta_c$ or $\delta > \delta_c$), a pronounced Drude peak reflects the mass enhancement in the Fermi liquid regimes that surround the QCP in the phase diagram; see Fig. 2(a). The behavior of $\sigma(\omega)$ at high energies, including the hybridization gap, is a generic feature of heavy-electron systems and is seen throughout the high-energy part of the phase diagram of Fig. 2(a).

responsible for the large mass enhancement and a small quasiparticle weight $z_L$; see Fig. 2(b). There is a small gap for the single-particle excitations at the wave vectors where the small Fermi surface would have resided.

- For $\delta < \delta_c$, the Fermi surface is small as determined by the conduction electrons alone. This is because when the amplitude of the static Kondo singlet vanishes, there is no longer a well-defined Kondo resonance. We refer to this state as a Kondo destruction ground state.
- At the QCP, single-particle excitations are gapless and have a non-Fermi-liquid form, at both small and large Fermi surfaces.

### A. High-energy excitations, temperature evolution, and mass enhancement

Figure 2(a) also contains a high-energy scale $T_0$ which describes the initial onset of dynamical Kondo correlations. This scale is generally affected by the presence of higher crystal electric field doublets (or quartets) that together form the $4f$ multiplet (Cornut and Coqblin, 1972; Kroha *et al.*, 2003; Chen *et al.*, 2017; Pal *et al.*, 2019). It is important to note that this scale smoothly evolves across the QCP at $\delta_c$. The development of the hybridization gap is associated with the initial onset of dynamical Kondo correlations, as illustrated in Fig. 3, and will appear on both sides of $\delta_c$.

For $\delta > \delta_c$, the temperature evolution of the physical properties reflects the flow of the system toward the Kondo screened ground state. For instance, the initial onset of dynamical Kondo correlations results in the Kondo screened ground state; the single-particle excitations develop into fully coherent heavy quasiparticles at the large Fermi surface as the temperature is lowered below $T_{\mathrm{FL}}$, the crossover temperature into the paramagnetic Fermi liquid state.

For $\delta < \delta_c$, the initial onset of dynamical Kondo correlations still takes place, even though it does not, in the end, lead to a well-defined Kondo resonance and the Kondo singlet amplitude vanishes in the ground state. Still, as the temperature is further lowered, vestiges of the Kondo effect will be observed at any nonzero temperature. In particular, the effective mass is a dynamical quantity, measuring the dispersion of the Landau quasiparticles, and is enhanced through the dynamical Kondo effect; further discussions of this point have been given by Si *et al.* (2014) and Cai *et al.* (2019).

### B. Isothermal evolution at low temperatures

The distinction between the two sides of $\delta_c$ can be sharply made at low temperatures, where well-defined quasiparticles reside at the small Fermi surface for $\delta < \delta_c$ and at the large Fermi surface for $\delta > \delta_c$. At zero temperature, a sudden reconstruction of the Fermi surface appears as $\delta$ passes through $\delta_c$. At nonzero but low temperatures, this becomes a crossover. The crossover width increases with increasing temperature. When the crossover width becomes large, the difference between the two sides becomes ambiguous. We illustrate this point next, especially through the experiments carried out on $YbRh_2Si_2$.

### C. Further considerations

In the Kondo destruction description, the *static* Kondo effect is suppressed in the antiferromagnetic phase at $\delta < \delta_c$. However, dynamical Kondo singlet correlations remain at nonzero frequencies in this regime. They lead to the development of $4f$-electron spectral weight near the Fermi energy, which we refer to as Kondo resonance-like features. The dynamical Kondo effect [see Cai *et al.* (2019) as well as earlier discussions by Zhu, Grempel, and Si (2003) and Si *et al.* (2014)] still produces a large mass enhancement and a small quasiparticle weight $z_S$; see Fig. 2(b). There is a small gap for the single-particle excitations at the wave vectors where the large Fermi surface would have developed.

The inelastic neutron scattering result on $CeCu_{6-x}Au_x$ ($x_c \approx 0.1$) (Schröder *et al.*, 2000) has been confirmed by the recent inelastic neutron scattering measurements (Poudel *et al.*, 2019) in $CeCu_{6-x}Ag_x$ ($x_c \approx 0.2$). When analyzing the data in terms of the one-component form, as arising in the Kondo destruction description, Poudel *et al.* (2019) found a similar form of $\omega/T$ scaling with a similar value for the critical exponent $\alpha = 0.73(1)$. Poudel *et al.* (2019) also analyzed the data in terms of a multicomponent spin fluctuation spectrum with one of the weaker components conforming to the expectation of an SDW QCP. However, thermodynamic singularities have provided evidence for the one-component description (Grube *et al.*, 2017).

### D. Summary of Sec. II

For heavy-electron metals, the Landau form of quantum criticality corresponds to an SDW QCP. A new type of

quantum criticality has been advanced in the form of a Kondo destruction (local) QCP. It goes beyond the Landau framework in that the critical destruction of Kondo entanglement characterizes the physics beyond the slow fluctuations of the magnetic order parameter. The Kondo destruction is characterized by a new energy scale $E^*_{\mathrm{loc}}$ vanishing at the QCP as illustrated in Fig. 2(a); a sudden reconstruction from large to small Fermi surface as the system is tuned from the paramagnetic side through the QCP, along with a vanishing quasiparticle weight on approach of the QCP from both sides, as illustrated in Fig. 2(b).

## III. ARPES, STM, AND THE SINGLE-PARTICLE GREEN'S FUNCTION

The unusual $\omega/T$ scaling of the dynamical spin susceptibility sets apart the QCP featuring critical Kondo destruction from the more traditional QCP based on the Landau framework of order-parameter fluctuations. It means that the dynamical susceptibility $\chi(\omega, T)$, in the regime where the critical singularities dominate, can be scaled to depend on $\omega$ or $T$ only through the combination $\omega/T$. Such scaling has been observed in $CeCu_{6-x}Au_x$ at its antiferromagnetic QCP (Schröder *et al.*, 1998) and indicated for $YbRh_2Si_2$ (Friedemann *et al.*, 2010). Recent measurements of the optical conductivity in thin films of $YbRh_2Si_2$ have demonstrated a singular response in the charge sector with an $\omega/T$ scaling (Prochaska *et al.*, 2020). A scaling form of this kind for both the optical conductivity and dynamical spin susceptibility is strongly suggestive of the presence of $\omega/T$ scaling in the single-particle excitations encoded in the single-particle Green's function.

### A. The single-particle Green's function

This Green's function can quite generally be cast into the form

$$G(\omega, \mathbf{k}, T) = \frac{1}{\omega - \varepsilon_{\mathbf{k}} - \Sigma(\omega, \mathbf{k}, T)}, \tag{2}$$

where $\varepsilon_{\mathbf{k}}$ is the bare electron dispersion and the proper self-energy $\Sigma(\omega, \mathbf{k}, T)$ encodes the effects of electron-electron interaction. In a Fermi liquid, this function can be decomposed into two parts,

$$G(\omega, \mathbf{k}, T) = G_{\mathrm{coh}}(\omega, \mathbf{k}, T) + G_{\mathrm{incoh}}(\omega, \mathbf{k}, T), \tag{3}$$

where the incoherent part is nonsingular close to the Fermi surface while the coherent part $G_{\mathrm{coh}}$ near $E_F$ describes the quasiparticle contribution and assumes the form

$$G_{\mathrm{coh}}(\omega, \mathbf{k}, T) = \frac{z}{\omega - v_F(k - k_F) + i\Gamma(\omega, T)}, \tag{4}$$

where $z$ is the quasiparticle weight and $v_F$ is the Fermi velocity. The lifetime of a quasiparticle is given by the inverse of the decay rate $\Gamma$. The amplitude of the static Kondo screening previously discussed is related to a pole in the self-energy, which in the Fermi liquid regime can at sufficiently low $\omega$ and $T$ be written as

$$\Sigma(\omega, \mathbf{k}, T) = \frac{a}{\omega - b} + \delta\Sigma(\omega, \mathbf{k}, T), \tag{5}$$

where $a$ and $b$ are parameters that capture the strength of Kondo screening and the energy of the Kondo resonance, respectively. The pole in $\Sigma$ shifts the Fermi momentum from its initial, "small" value to a new, "large" value as long as $a \neq 0$. In the SDW QCP case, $a \neq 0$ on either side of the critical point. For the local QCP, by contrast, Kondo screening is critically destroyed; correspondingly, on the antiferromagnetic side, $a = 0$ and the Fermi surface is small.

The Hall effect turns out to be a particularly useful quantity in this context as it is a measure of the carrier density on either side of the QCP. This is a consequence of the Fermi liquid nature of the two phases separated by the QCP, in which the Hall coefficient is completely determined by the renormalized dispersion of the single-particle excitations, to the leading order of elastic scattering (quenched disorder) when it is nearly isotropic. In other words, here, the Hall coefficient is independent of the quasiparticle weight $z$ or any Landau parameters, regardless of the strength of electron-electron (and electron-phonon) interactions. This can be seen through the kinetic equations of a Fermi liquid or using the Kubo formalism (Betbeder-Matibet and Nozières, 1966; Kohno and Yamada, 1988) and related Feynman diagrammatic means (Khodas and Finkel'stein, 2003).

The dynamical spin susceptibility $\chi(\omega, \mathbf{k}, T)$ and also the optical conductivity $\sigma(\omega, T)$ can be written as convolutions of the Green's function with itself and specific vertex functions. On the other hand, ARPES and STM measurements depend directly on $G(\omega, \mathbf{k}, T)$. Single-particle spectroscopies are thus, at least in principle, particularly useful in distinguishing between the two types of quantum criticality.

### B. ARPES and STM

ARPES and STM measurements probe the single-particle spectrum and thus give access to the spectral function $A(E, \mathbf{k}) = -(1/\pi)\mathrm{Im}G(\omega = E + i0^+, \mathbf{k}, T)$. Although the single-particle Green's function appears in the theoretical description of ARPES and STM, both spectroscopic techniques are complementary. While ARPES directly probes the single-particle excitations as a function of energy and momentum, STM measures a conductance that is local in real space. Both methods are surface sensitive, albeit to different degrees. Furthermore, through variation of the photon energy, the bulk sensitivity of ARPES can be enhanced. By construction, ARPES probes only the occupied part of the single-particle excitation spectrum, which, especially at low temperatures, leads to a sharp cutoff at the Fermi energy (Hüfner, 2003). ARPES therefore measures only part of the full spectral function, i.e., the imaginary part of the retarded Green's function below the Fermi energy. A sketch of the spectral function of a Fermi liquid is shown in Fig. 4(a). It consists of contributions from the quasiparticle pole and an incoherent background. The quasiparticle pole contributes a factor $z$ to the total area beneath the spectral function, while the incoherent background contributes $1 - z$ times the total area. $z$ is commonly called the wave-function renormalization factor and it is inversely proportional to the quasiparticle mass in a Fermi liquid. The evolution of $z$ with tuning parameter is plotted schematically in Fig. 2(b) where we see that $z$ vanishes at a local QCP. The position of the quasiparticle pole as a

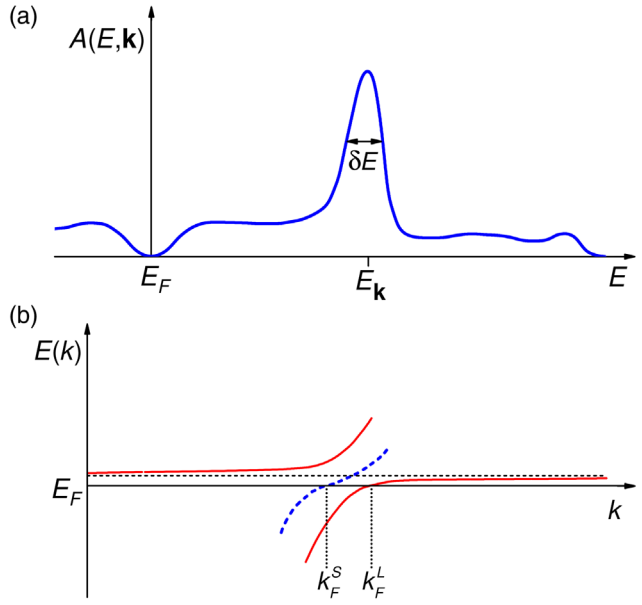


FIG. 4. Electronic characteristics of the Fermi liquid state of a Kondo lattice. (a) Spectral density of a Fermi liquid: The quasiparticle pole at $E_{\mathbf{k}}$ has a characteristic width $\delta E$ that increases with the distance from the Fermi energy $E_F$ as $\delta E \sim |E_{\mathbf{k}} - E_F|^2$. A similar broadening occurs due to finite temperature effects. The incoherent part of $A(E, \mathbf{k})$ vanishes at $E_F$. (b) Quasiparticle dispersion in the Fermi liquid to either side of the QCP: $k_F^L$ and $k_F^S$ refer to large and small Fermi surfaces, respectively. Across a Kondo destruction QCP, the one-electron spectrum is gapless at $k_F^L$ and develops a small gap at $k_F^S$ for $\delta > \delta_c$, and the converse is valid for $\delta < \delta_c$. The flattening of the dispersion near $k_F^S$ for $\delta < \delta_c$ (dashed blue curve) reflects the effective mass enhancement due to the dynamical Kondo effect.

function of momentum defines the disperion. *Per se*, ARPES is not able to distinguish between the quasiparticle peak and the incoherent part of the spectral function. Provided the energy and momentum resolution is not a limiting factor, however, the characteristic broadening $\delta E$ of the quasiparticle peak in energy ($\sim|E_{\mathbf{k}} - E_F|^2$, where $E_{\mathbf{k}}$ is the quasiparticle energy) and with temperature ($\sim T^2$) should be discernible in the momentum-distribution curves provided by ARPES. The weight of the quasiparticle peak, in principle, could also be extracted based on the total incoherent part. However, since ARPES probes only occupied states, the complete spectral function is inaccessible. Although inverse photoemission is in principle able to probe states above the Fermi energy, it is limited by rather poor energy resolution.

In general, when interpreting ARPES spectra, one needs to keep in mind that in order to relate the photoemission intensity to the spectral function, the one-electron dipole matrix element enters, which generally is unknown. In addition, $k_z$ broadening can be important, where $k_z$ is the component of the electron momentum perpendicular to the surface and depends on the photon energy (Strocov, 2003; Wadati *et al.*, 2006).

STM, on the other hand, measures a local-in-real-space conductance. In the linear-response regime, the current-voltage characteristics are related to the local density of states (DOS) of the material under investigation (Bardeen, 1961; Tersoff and Hamann, 1985). Therefore, at low bias voltage and temperature, the spatially resolved spectral density can be obtained. As the applied bias voltage shifts the chemical potential at which the local density of states is probed, STM is, unlike ARPES, not confined to only occupied states. It is, however, important to realize that the assumption that the spectral function is independent of the bias voltage has to break down at some sample-dependent value of the bias voltage beyond which the tunneling current can no longer be related to the local density of states. Moreover, the properties of the STM tip, e.g., its DOS, may affect the results.

### C. Probing quantum criticality in the Kondo lattice

One of the strongest diagnostic tools to distinguish the local QCP from the SDW QCP is Hall conductivity measurements as the local QCP manifests itself by a jump of the Hall coefficient across the QCP. This is a consequence of the Hall coefficient being inversely proportional to the carrier density (in the isotropic case or, in general, the curvatures of the quasiparticle dispersion on the Fermi surface) while being independent of the quasiparticle weight $z$ in a Fermi liquid. The continuous nature of the local QCP is ensured by the vanishing of the quasiparticle weight from either side of the transition. For an SDW QCP, on the other hand, $z$ will remain nonzero (except at isolated points on the Fermi surface) as $\delta$ is tuned through $\delta_c$.

In a Kondo lattice at sufficiently high temperatures, where in first approximation the effect of the RKKY interaction can be ignored, the single-impurity Anderson model is expected to capture the overall physical behavior. This model is given by

$$H_{\mathrm{AND}} = \sum_{\sigma} \varepsilon f_{\sigma}^{\dagger} f_{\sigma} + \sum_{\mathbf{k},\sigma} \varepsilon_{\mathbf{k}} c_{\mathbf{k},\sigma}^{\dagger} c_{\mathbf{k},\sigma} + \frac{U}{2} \sum_{\sigma \neq \sigma'} f_{\sigma}^{\dagger} f_{\sigma'}^{\dagger} f_{\sigma'} f_{\sigma} + \sum_{\mathbf{k},\sigma} (V_{\mathbf{k}} f_{\sigma}^{\dagger} c_{\mathbf{k},\sigma} + \mathrm{H.c.}), \quad (6)$$

where $f_{\sigma}^{\dagger}$ ($f_{\sigma}$) is the set of local $4f$ electron creation (destruction) operators of spin projection $\sigma$. The conduction electron operators are $c_{\sigma}^{\dagger}$ and $c_{\sigma}$. The band structure of the conduction electrons is encoded in $\varepsilon_{\mathbf{k}}$, and the matrix element $V_{\mathbf{k}}$ that mixes $4f$ and $c$ electrons is referred to as the hybridization. [For the case of the periodic Anderson model in the local-moment limit, with the $4f$ electron occupancy being close to unity, it reduces to the Kondo lattice model given in Eq. (1) when the charge degrees of freedom of the $4f$ electrons are projected out (Schrieffer and Wolff, 1966; Zamani, Ribeiro, and Kirchner, 2016a).]

STM spectra of single-site Kondo problems possess the structure of Fano resonances (Fano, 1961) and depend on the ratio of tunneling into the Kondo impurity versus tunneling into the embedding host. This ratio is encoded in the so-called Fano parameter. Rigorous derivations of the tunneling current and the form of the Fano parameter are given by Schiller and Hershfield (2000), Újsághy *et al.* (2000), and Plihal and Gradzuk (2001). If tunneling occurs predominantly into the conduction band the measured local DOS features the suppression of conduction electron states near the Fermi energy as the Kondo effect develops. The first scanning tunneling studies of dense Kondo systems appeared about a

decade ago (Aynajian *et al.*, 2010; Ernst *et al.*, 2010; Schmidt *et al.*, 2010). The pronounced variation of STM spectra with the type of surface for Kondo lattice compounds is largely due to variations in the Fano parameter (see, e.g., Fig. 10 for tunneling into differently terminated surfaces). This has been explicitly demonstrated based on mean field and dynamical mean field theory approximations for the Kondo lattice (Maltseva, Dzero, and Coleman, 2009; Figgins and Morr, 2010; Wölfle, Dubi, and Balatsky, 2010; Benlagra, Pruschke, and Vojta, 2011). At sufficiently high temperatures, however, STM spectra in the vicinity of each Ce moment are expected to be similar to those for the single-ion Kondo case. Kondo screening is a predominantly local phenomenon and thus its onset and evolution are easily probed in real space, i.e., via STM. For a study of the single-particle Green's function in the paramagnetic Fermi liquid regime of the Kondo lattice far away from any QCP, in the context of photoemission, see Reinert *et al.* (2001) and Costi and Manini (2002). ARPES measurements at similar temperatures, around and above the energy scale $T_0$, provide the band structure $\varepsilon_{\mathbf{k}}$ of the occupied conduction electron states. A flat band near the $4f$ electron atomic level $\varepsilon$ [see Eq. (6)], which is far from the Fermi energy, and the formation of a flat band near the Fermi energy induced by the Kondo effect at each Ce moment reflect the $4f$ electron spectral weight. This can be enhanced using resonant ARPES (Chen *et al.*, 2017).

At sufficiently low temperatures, in the Fermi liquid regime to either side of the QCP at $\delta_c$ [Fig. 2(a)], the band structure near the Fermi energy is shown in Fig. 4(b). For $\delta < \delta_c$, the small Fermi surface prevails and the band structure is that of the blue dashed line crossing the Fermi energy $E_F$ at $k_F^S$. Still, incoherent spectral weight, a vestige of incomplete Kondo screening, develops but is ultimately gapped near $k_F^L$. For $\delta > \delta_c$, the Fermi surface incorporates the $4f$ moments and the Fermi wave vector changes from $k_F^S$ at high temperatures (without the $4f$ moments) to $k_F^L$ at low temperatures. On this side of the QCP, any spectral weight near $k_F^S$ is due to incoherent single-particle excitations and is ultimately gapped. In other words, for $\delta > \delta_c$ in the Fermi liquid regime the spectral weight near the dashed blue line of Fig. 4(b) has developed a small gap at $k_F^S$. This should in principle be directly detectable via ARPES, provided the energy and momentum resolution are sufficiently high, and low enough temperatures can be reached.

On the other hand, the change $k_F^S$ to $k_F^L$ has only indirect vestiges in real space as the Fermi liquid is a momentum-space concept. The ensuing difficulties when tracing single-particle excitations in real space can already be read off from Fig. 4(b): The Fermi liquid is described by a low-energy effective theory and is valid only in the vicinity of $k_F$. [The spectral function is a more general concept but it only assumes a form as illustrated in Fig. 4(a) in the Fermi liquid regime.] Fourier transforming the momentum-resolved spectral function to real space necessarily will sum up spectral weight outside of the Fermi liquid regime, where the characteristic form of broadening that identifies the quasiparticle peak is no longer valid.

One possible way forward is to perform quasiparticle interference (QPI) experiments to map out the band structure near the Fermi energy (Derry, Mitchell, and Logan, 2015; Yazdani, da Silva Neto, and Aynajian, 2016). We return to this possibility in Sec. VI. Another possible way is to perform isothermal STM measurements at low temperatures through the phase diagram connecting $\delta < \delta_c$ with $\delta > \delta_c$. While this by itself does not provide any direct information on the size of the Fermi surface, it was recently demonstrated that such a measurement is able to pick up the critical slowing down at the Kondo destruction energy scale (Seiro *et al.*, 2018) as discussed in Sec. IV.

### D. Summary of Sec. III

The nature of quantum criticality in heavy-electron metals is manifested in the evolution of the single-particle excitations across the QCP. It is natural to probe this behavior using the ARPES and STM spectroscopies, given that they are an established means of studying single-particle excitations in metals. However, this task is challenging, mostly because heavy-electron systems have the distinction that the required energy scale is very low.

For ARPES, this requirement poses a challenge to access the quantum-critical behavior as is the limitation that even the state-of-the-art setups cannot yet reach temperatures below about 1 K. Still, ARPES should be informative in elucidating (i) the onset of a hybridization gap, which represents the high-energy physics for the quantum criticality of heavy-electron metals [see Fig. 2(a)]; and (ii) the evolution of the dynamical Kondo effect as temperature is lowered toward either the antiferromagnetic or paramagnetic ground state or the quantum-critical regime.

STM spectroscopy has superb energy resolution and can reach low temperatures, but more demanding setups (such as those suited for QPI) are needed to access the information in the momentum space. Still, STM probes the single-particle physics in a way that is complementary to ARPES. In addition, it provides a promising means to probe the isothermal evolution of single-particle excitations at low temperatures across the Kondo destruction energy scale.

## IV. QUANTUM CRITICALITY IN $YbRh_2Si_2$

$YbRh_2Si_2$ is a prototype system for local quantum criticality as illustrated by its temperature ($T$)–magnetic field ($B$) phase diagram; see Fig. 5(a). Here the Fermi surface jump and the Kondo destruction energy scale have been extensively studied through magnetotransport and thermodynamic measurements. At a given temperature, the isothermal Hall coefficient [Fig. 5(b)] and other transport and thermodynamic quantities display a rapid crossover (Paschen *et al.*, 2004; Gegenwart *et al.*, 2007; Friedemann *et al.*, 2010).

From these measurements, a $E^*(B)$ line is thus specified in the phase diagram. This line relates to each $T$ a $B^*$ scale: $B^*(T) \geq B_c$ with $B^*(T=0) = B_c$. The full width at half maximum (FWHM) of the crossover [Fig. 5(b)] extrapolates to zero in the zero-temperature limit [Fig. 5(d)], which implicates a jump of the Fermi surface across the QCP. It follows that, in the low-temperature limit, at $B < B_c$, the Fermi surface is small.

On the nonmagnetic side, $B > B_c$, the mass enhancement diverges as $B$ approaches $B_c$ from above. This has been established by measurements of both the $T$-linear specific-heat

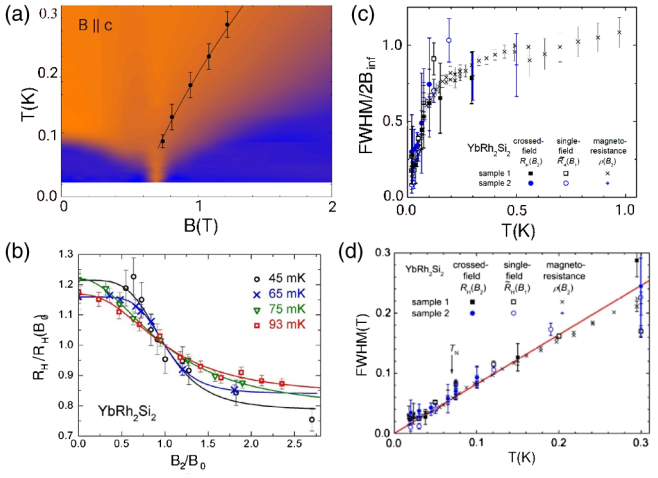


FIG. 5. Quantum criticality in $YbRh_2Si_2$. (a) The temperature vs field phase diagram of $YbRh_2Si_2$. The blue regions mark Fermi liquid behavior, i.e., $\rho(T)-\rho(0)\sim T^2$, while orange indicates the quantum-critical area of the phase diagram where $\rho(T)-\rho(0)\sim T^x$, with $x\approx 1$. The continuous line in the quantum-critical region is the $E^*$ line as derived from thermodynamic and transport properties (Paschen *et al.*, 2004; Gegenwart *et al.*, 2007; Friedemann *et al.*, 2010). Adapted from Custers *et al.*, 2003. (b) Normalized Hall coefficient across the critical field for different temperatures. The inverse of $R_H$ is a measure of the carrier density. The lower $T$, the sharper is the crossover. At $T=0$ and $B=B_c$, a jump of $R_H$ corresponds to the sudden localization of $4f$ electrons as $B$ is taken trough $B_c$ from above. From Paschen *et al.*, 2004. (c) Comparison between the isothermal magnetotransport crossover width and the crossover field as specified by the ratio of the FWHM/2 to the crossover inflection field $B_{\rm inf}$. FWHM denotes the full width at half maximum. From Paschen *et al.*, 2016. (d) The "sharpness" of the crossover: The FWHM vanishes in a linear-in-$T$ fashion indicating a jump of $R_H$ at $B_c$ in the zero-temperature limit. From Friedemann *et al.*, (2010).

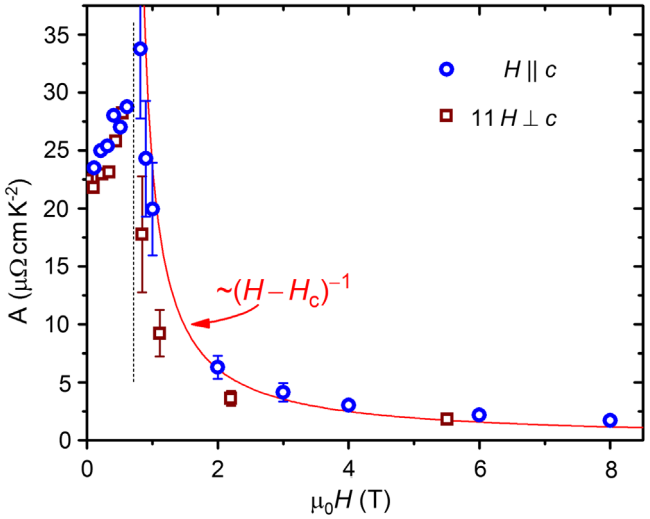


FIG. 6. Divergence of the $T^2$ coefficient $A$ of the resistivity at the QCP in $YbRh_2Si_2$. Through the Kadowaki-Woods relation, this implies that the effective mass diverges on approach to the critical field $B_c=\mu_0 H_c$ from either side of the QCP. Data for $H\perp c$ have been scaled by a factor of 11. Adapted from Gegenwart *et al.*, 2002.

coefficient $\gamma$, which is proportional to the effective mass $m^*$, and the $T^2$ coefficient $A$ of the resistivity, which was found to obey the Kadowaki-Woods relation (Tsujii, Kontani, and Yoshimura, 2005). The divergence of $A$ is shown in Fig. 6.

For $B<B_c$, the mass enhancement is also large. This is compatible with the large $C/T$ measured in the antiferromagnetic state, although to reliably extract $\gamma$ is a challenge because of the interference of the large specific-heat feature at the magnetic transition temperature $T_N$. The mass enhancement can be more reliably extracted from the $A$ coefficient, because the effect of the magnetic transition at $T_N$ on the resistivity is relatively minor. The evolution of the $A$ coefficient with $B$ is consistent with the destruction of the Kondo effect as the QCP is approached from the nonmagnetic side as well as the dynamical Kondo effect inside the antiferromagnetic phase.

The effect of increasing temperature on the Hall crossover can be quantified in terms of the ratio of the crossover width to the crossover magnetic field. For $T\gtrsim 0.5$ K, the ratio quickly increases toward unity as shown in Fig. 5(c). This implies that, for such temperatures, $YbRh_2Si_2$ falls in the quantum-critical fluctuation regime already for zero magnetic field. Thus, the single-particle spectral weight will be significant at both the small and large Fermi surfaces. In this temperature range, significant spectral weight is thus to be expected at the large Fermi surface. The ARPES measurements in $YbRh_2Si_2$, which have been reported for $T>1$ K (Kummer *et al.*, 2015), are consistent with this prediction (Paschen *et al.*, 2016).

The temperature evolution of the single-particle excitations in $YbRh_2Si_2$ has been studied by STM measurements, which were first carried out down to 4.6 K by Ernst *et al.* (2011) and were recently extended down to 0.3 K (Seiro *et al.*, 2018). The lattice Kondo effect has been identified with the feature at a particular bias −6 meV. The initial onset of this feature takes place near 25 K, which corresponds to $T_0^{\rm en}$, an estimate of $T_0$ based on the spin entropy $S$ and defined through $S(T_0^{\rm en}/2)=0.4R\ln 2$, where $R$ is the ideal gas constant; see Table I. At $B=0$, the measurements down to $T=0.3$ K show an increase in the spectral weight; see Fig. 7(a). This is compatible with the dynamical Kondo effect at nonzero temperatures.

The STM experiments have also determined the isothermal $B$ dependence of the peak width at the lowest measured temperature $T=0.3$ K. It shows a minimum near $B^*(T=0.3\ \text{K})$ as shown in Fig. 7(b). This observation is consistent with a critical slowing down associated with the Kondo destruction energy scale that was implicated by magnetotransport and thermodynamic measurements (Paschen *et al.*, 2004; Gegenwart *et al.*, 2007; Friedemann *et al.*, 2010). As such, it represents the most direct evidence so far for the Kondo destruction quantum criticality based on a single-particle measurement in $YbRh_2Si_2$.

### A. Summary of Sec. IV

We now summarize the salient results on $YbRh_2Si_2$ discussed in this section.

*High-energy features:* STM experiments for $YbRh_2Si_2$ at $B=0$ clearly observe the initial onset of dynamical Kondo

TABLE I. Characteristic high- and low-temperature scales for several heavy-electron compounds located in the vicinity of quantum criticality. Here $T_{\mathrm{FL}}$ is a temperature scale below which the Landau Fermi liquid $T^2$ resistivity is observed. $T_0^{\mathrm{hyb}}$ is a "high-temperature" estimate for the onset of the hybridization gap and is estimated from the optical conductivity $\sigma(\omega, T)$ (Figs. 3 and 13) with the exception of $CeRhIn_5$, where existing $\sigma(\omega, T)$ data indicate only that $8 < T_0^{\mathrm{hyb}} < 300$ K (Mena, van der Marel, and Sarrao, 2005). $T_0^{\mathrm{en}}$ is a "low-temperature" estimate of $T_0$ based on the spin entropy $S$, using a procedure for the single-impurity Kondo model with constant conduction electron density of states (for which $T_0 = T_0^{\mathrm{en}} = T_K^0$): $S(T_0^{\mathrm{en}}/2) = 0.4R\ln 2 \approx 0.277R$, where $R = 8314.5$ mJ/(mol K) is the ideal gas constant. LMT designates the lowest measured temperature for the electrical resistivity $\rho$. For $YbRh_2Si_2$ at the critical field, $T_{\mathrm{FL}}$ has been estimated from $\rho(T)$ and using the result that $\rho(T) \sim T$ down to the LMT of 8 mK (Taupin *et al.*, 2015), making the listed value to be an upper bound. The hybridization-gap onset in $\sigma(\omega)$ is assumed to be the same for $0 \le B \le 2$ T. Similarly, changes of $T_0^{\mathrm{en}}$ are assumed to be small for fields $0 \le B \le 2$ T, where the specific heat at around 20 K is only weakly field dependent for $B \le 2T$ (Gegenwart *et al.*, 2006). For $CeRhIn_5$, the QCP is located at $p_c = 2.35$ GPa and $H_c$ with $\mu_0 H_c \lessapprox 10$ T (Park *et al.*, 2008). For $CeCu_{6-x}Au_{0.1}$, $\rho(T)$ is linear in $T$ down to the LMT of 20 mK; hence, the listed value is also an upper bound. The estimate of $T_0^{\mathrm{hyb}}$ in $CeCu_{6-x}Au_{0.1}$ is supported by the specific-heat data of Löhneysen *et al.* (1994). The references in this table are arranged such that in each row the first reference provides $T_{\mathrm{FL}}$, the second contains estimates for $T_0^{\mathrm{hyb}}$, and the third provides results on the low-temperature (spin) entropy.

| | $T_{\mathrm{FL}}$ (K) | $T_0^{\mathrm{hyb}}$ (K) | $T_0^{\mathrm{en}}$ (K) | Reference |
|---|---|---|---|---|
| $YbRh_2Si_2$ | 0.07 | ∼160 | ≈24 | Gegenwart *et al.* (2006), Kimura *et al.* (2006), and Trovarelli *et al.* (2000) |
| $YbRh_2Si_2$ ($B = B_c$, $B\|c$) | < 0.008 (LMT) | ∼160 | ≈24 | Gegenwart *et al.* (2006), Kimura *et al.* (2006), and Taupin *et al.* (2015) |
| $YbRh_2Si_2$ ($B = 2$ T, $B\|\ c$) | 0.135 | ∼160 | ≈24 | Gegenwart *et al.* (2002, 2006), and Kimura *et al.* (2006) |
| $CeCoIn_5$ | 0.14 ($B = 6$ T) | ≳100 | ≈25 | Mena, van der Marel, and Sarrao (2005), Paglione *et al.* (2007), and Petrovic, Pagliuso *et al.* (2001) |
| $CeRhIn_5$ | < 0.15 ($p_c = 2.35$ GPa, $\mu_0 H = 10$ T) | ≳60[a] | ≈10 | Chen *et al.* (2018b), Park *et al.* (2008), and Park and Thompson (2009) |
| $CeCu_6$ | 0.2 | ≳40 | ≈4 | Amato *et al.* (1987), Fischer *et al.* (1987), and Marabelli and Wachter (1990) |
| $CeCu_{6-x}Au_x$ ($x_c = 0.1$) | < 0.02 (LMT) | ≳40 | ≈4 | Fischer *et al.* (1987), Löhneysen *et al.* (1994), and Marabelli and Wachter (1990) |

[a]This value for $T_0^{\mathrm{hyb}}$ has been estimated from the ARPES data of Chen *et al.* (2018b) for ambient conditions; see also Fig. 12.

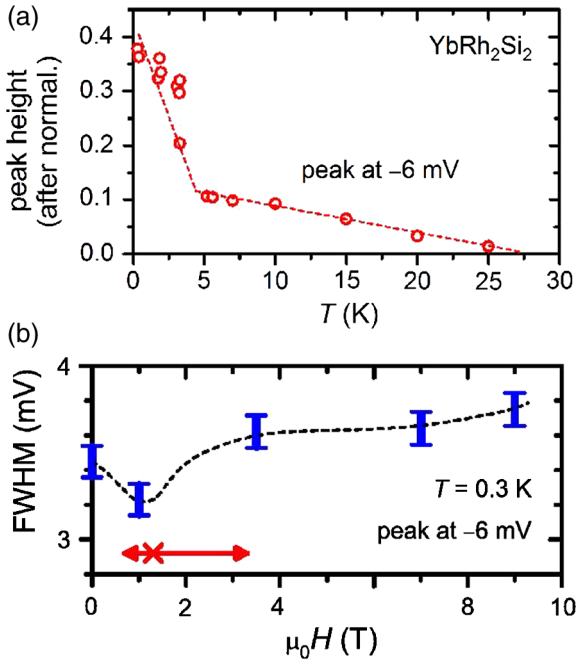


FIG. 7. STM spectroscopy of the lattice Kondo feature at −6 meV in $YbRh_2Si_2$. (a) The temperature evolution of the peak height of the −6 meV peak. A strong increase in the peak height is observed below 5 K. (b) The FWHM of the −6 meV peak across the critical field at the base temperature $T = 0.3$ K. Note that at this temperature all field values place the system within the quantum-critical fan. The decrease of the peak width near $B^* = \mu_0 H^*(T = 0.3\ \mathrm{K})$ is consistent with a critical slowing down at quantum criticality. From Seiro *et al.*, 2018.

correlations around $T_0$, a comparatively high temperature, as expected for any Kondo lattice system regardless of the nature (Kondo screened or Kondo destruction) of its ground state. This is consistent with the observation of a hybridization gap in the optical spectrum (Kimura *et al.*, 2006). As temperature is further lowered below $T_0$, $4f$ electron spectral weight is expected to develop, and this has also been clearly observed.

*Low-energy isotherms:* STM experiments for $YbRh_2Si_2$ have been carried out as a function of magnetic field at $T = 0.3$ K. The Kondo lattice spectral peak shows a critical slowing-down feature at $B^*$, the Kondo destruction scale previously determined from magnetotransport and thermodynamic measurements. As such, the STM results are consistent with local quantum criticality.

## V. THE CERIUM-BASED 115 FAMILY: PHOTOEMISSION VERSUS TUNNELING SPECTROSCOPY

The cerium-based 115 family is comprised of compounds $CeMIn_5$ where $M =$ Co, Rh, or Ir. These compounds are stoichiometric and can be grown in a very clean form. All three compounds crystallize in the $HoCoGa_5$ structure type and thus possess tetragonal unit cells. Because of their proximity to quantum criticality, they have contributed considerably to a global understanding of quantum-critical heavy-electron materials (Si, 2006; Park and Thompson, 2009). While $CeCoIn_5$ and $CeIrIn_5$ under ambient conditions are low-temperature superconductors, $CeRhIn_5$ is an antiferromagnet (Movshovich *et al.*, 2001; Petrovic, Pagliuso *et al.*,

2001). In addition, substituted variants, e.g., by Cd substitution on the In site or by substitution of Ce, have also been investigated; for a review, see Thompson and Fisk (2012).

### A. $CeIrIn_5$

$CeIrIn_5$ at ambient pressure is a heavy-electron superconductor with a transition temperature $T_c = 0.40$ K (Petrovic, Movshovich *et al.*, 2001). After almost two decades of study, the origin of superconductivity remains controversial, although there is growing support for a magnetically driven mechanism (Chen *et al.*, 2015). In spite of this controversy, superconductivity in $CeIrIn_5$ has attracted recent attention because of its unusual strain tunability (Bachmann *et al.*, 2019).

In contrast to $CeCoIn_5$ or even $CeRhIn_5$, $CeIrIn_5$ has been comparatively less studied by STM and ARPES. Early ARPES studies led to different conclusions concerning the formation of $4f$-derived flat bands (Fujimori *et al.*, 2003, 2006). More recently, a high-resolution ARPES study by Chen *et al.* (2018a) mapped out the full band structure of $CeIrIn_5$. Interestingly, this study was able to resolve the complete fine structure of both the $4f^1_{5/2}$ and $4f^1_{7/2}$ peaks in the measured energy-distribution curves (EDCs) and momentum-distribution curves, which may be a reflection of the comparatively stronger $4f-c$ hybridization than in $CeCoIn_5$ (Chen *et al.*, 2018a).

To the best of our knowledge, no scanning tunneling spectroscopy of $CeIrIn_5$ is available, apart from an STM investigation that focused on the structural properties of $CeIrIn_5$ surfaces (Ernst *et al.*, 2010; Wirth *et al.*, 2014). Our main focus in this section is therefore on $CeCoIn_5$ and $CeRhIn_5$.

### B. $CeCoIn_5$

$CeCoIn_5$ has attracted interest not only for its comparatively high superconducting transition temperature $T_c \sim 2.3$ K but also for an overall phenomenology that resembles that of the underdoped cuprates.

The strong interest in $CeCoIn_5$ includes early photoemission studies which, however, have led to contradictory results concerning the localized versus itinerant nature of the $4f$ electrons (Koitzsch *et al.*, 2008, 2009, 2013). Optical conductivity measurements of $CeCoIn_5$ show the existence of a hybridization gap at high energies which starts forming at comparatively high temperatures (Singley *et al.*, 2002; Burch *et al.*, 2007) and recent STM studies of $CeCoIn_5$ are in line with these findings (Aynajian *et al.*, 2012; Allan *et al.*, 2013; Zhou *et al.*, 2013). de Haas–van Alphen (dHvA) studies performed at low temperatures indicate that the Fermi surface of $CeCoIn_5$ includes the $4f$ electrons and that therefore the Fermi surface of $CeCoIn_5$ is large (Settai *et al.*, 2001; Shishido *et al.*, 2002). This conclusion is further corroborated by band-structure calculations that treat the $4f$ electrons as fully itinerant (Haule, Yee, and Kim, 2010).

$CeCoIn_5$ under ambient conditions is believed to be located close to an antiferromagnetic QCP of the SDW type and can be tuned to a quantum phase transition by applying a magnetic field (Ronning *et al.*, 2005; Singh *et al.*, 2007; Zaum *et al.*, 2011). The STM study by Aynajian *et al.* (2012) also reported an interesting energy-over-temperature ($\omega/T$) scaling of the local conductance of $CeCoIn_5$ which sets in around 60 K. It is worth recalling that STM probes the single-particle response while the dynamical spin susceptibility measures the magnetic fluctuation spectrum. As $\omega/T$ scaling is not expected in the dynamical spin susceptibility at a QCP of the SDW type, the observation of dynamical scaling in the local conductance suggests that the SDW nature applies, at least at ambient conditions, only at asymptotically low energies. In any case, the observation of $\omega/T$ scaling does appear to be in line with the linear-in-temperature behavior of the resistivity below 20 K (Petrovic, Pagliuso *et al.*, 2001) as shown in Fig. 8. Further support in favor of such an $\omega/T$ scaling in $CeCoIn_5$ for the single-particle excitations near the $\Gamma$ point has come from a recent high-resolution ARPES study (Chen *et al.*, 2017).

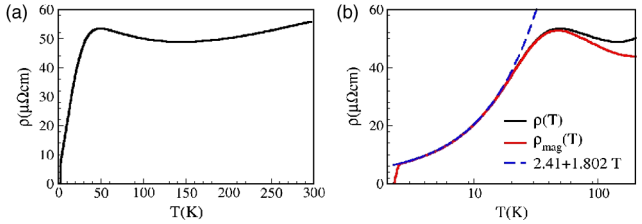


FIG. 8. Temperature dependence of the resistivity $\rho$ of $CeCoIn_5$. (a) $\rho(T)$ in the temperature range from 2.2 to 300 K. $\rho$ has a smooth maximum around $T_{\rm coh} \approx 40$ K; this temperature for the resistivity maximum is commonly referred to as the coherence temperature, which is a manifestation of $T_0$ defined earlier. (b) $\rho$ (black continuous line) and the magnetic resistivity $\rho_m$ (red continuous line) in a semilog plot for temperatures from 2 to 200 K. $\rho_m(T)$ is defined as the difference between the resistivity of $CeCoIn_5$ and that of its nonmagnetic reference compound $LaCoIn_5$ at temperature $T$. The dashed line represents a linear law fit to $\rho_m(T)$ and shows that $\rho_m(T)$ is linear in $T$ from $T_c$ to approximately 20 K.

The ARPES study by Chen *et al.* (2017) reported the first 3D Fermi surface mapping of $CeCoIn_5$ and provided a measurement of the full band structure of this heavy-electron system. Because of the large temperature range of the study from 14 to 310 K, Chen *et al.* were able to demonstrate that the formation of the $4f$-derived flat band sets in at temperatures far above the coherence temperature. This finding is significant, although not entirely unexpected. It demonstrates not only the slow evolution of the Kondo screening process but also the likely role of a Kondo effect on the excited crystal field levels (Chen *et al.*, 2017; Pal *et al.*, 2019). These results contrast with a temperature-independent Fermi surface in $YbRh_2Si_2$ that was inferred from the state-of-the-art ARPES measurements in a temperature window from 1 to 100 K (Kummer *et al.*, 2015). An earlier laser-based ARPES study of $YbRh_2Si_2$ reported a $T$-dependent band structure below 100 K (Mo *et al.*, 2012). In this regard, we note that Chen *et al.* (2017) suggested that ARPES at temperatures larger than 100 K may be required in $YbRh_2Si_2$ due to the large effect of the crystal field levels. This is consistent with $T_0^{\rm hyb} \approx 160$ K in this compound; see Table I.

High-resolution ARPES results on $CeCoIn_5$ that are largely compatible with those of Chen *et al.* (2017) have also been reported by Jang *et al.* (2017). Although ARPES measurements on heavy-electron compounds have been a major

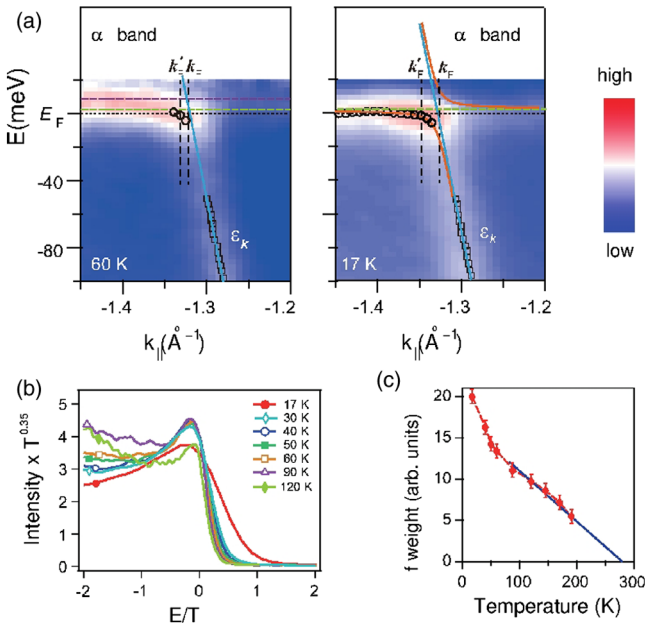


FIG. 9. ARPES view of the $4f$ electron weight near the Fermi energy in $CeCoIn_5$. (a) Evidence for the initial development of hybridization between $4f$ and conduction band $\alpha$ at $T = 60$ and 17 K after dividing the EDCs by the Fermi-Dirac function. (b) $\omega/T$ scaling of the EDCs near the Γ point in an intermediate temperature range and energy range around the Fermi energy $E_F$. (c) Background subtracted $4f$ electron spectral weight transfer near the Γ point vs temperature. The EDCs have been integrated over an energy window from −40 to 2 meV. From Chen *et al.*, 2017.

experimental achievement, care has to be taken when extrapolating to the high-temperature region where the $4f$ electrons have to be localized across the phase diagram as previously argued. In Fig. 9(a) we reproduced the EDCs from Chen *et al.* (2017) for the $\alpha$ band, one of three bands that are part of the high-temperature Fermi surface, in the vicinity of its Fermi crossing for both $T = 60$ and 17 K. The data have been divided by the Fermi-Dirac function to access the region (slightly) above the Fermi energy. The dashed lines in Fig. 9(a) indicate the positions of maxima of the main and the first excited crystal electric field-related Kondo resonancelike features, both of which are taken to be dispersionless. Here $k_F$ is the Fermi momentum of the conduction electrons without $4f$ participation, i.e., at high temperatures.

In Fig. 9(c), the building up of spectral weight near the Fermi energy is shown as a function of temperature. This is calculated by integrating the EDCs near the Fermi energy, i.e., from −40 to 2 meV, and after subtracting a flat, temperature-independent overall background. It is worth recalling that the majority of the Kondo resonancelike features of a cerium-based system is located above the Fermi energy, a region which is, especially at low $T$, inaccessible to ARPES.

It is instructive to analyze the high-resolution ARPES data of Chen *et al.* for the temperature-dependent band structure of $CeCoIn_5$ in light of the expectation that the Fermi surface of this compound should contain the $4f$ electrons at sufficiently low temperatures. In other words, in terms of Fig. 2, $CeCoIn_5$ is located on the $\delta > \delta_c$ side of the $E^*_{\rm loc}$ line. Note, however, that Fig. 2 presents one type of specific cut through the global heavy-electron phase diagram (Si, 2006); its variant, with $E^*_{\rm loc}$ at $\delta_c$ being small but nonzero, is believed to describe $CeCoIn_5$.

The continuous red line in the right-hand panel of Fig. 9(a) is a fit of the data to the mean field expression for the single level, single band Anderson lattice model. The circles in Fig. 9(a) are obtained from the maximum in the EDCs and interpreted as the dispersion of the quasiparticle band. This leads to the value of $k'_F$, where $k'_F$ is the projected zero-temperature Fermi momentum. Such a fit should not be taken too literally. As previously mentioned, mean field approaches may in principle be suitable to address the conduction bands at comparatively high energies and temperatures or the low-energy behavior on either the small or the large Fermi volume side in a limited energy range. They do, however, generically fail to describe the crossover from the high- to the low-energy or temperature behavior. In addition, there is the general difficulty of constructing the correct mean field theory. The effective model for a system like $CeCoIn_5$ should not be the single level, single band Anderson lattice model. Nonetheless, the mean field construction provides an estimate for the change in the Fermi wave vector from its high-temperature value $k_F$ to $k'_F$. If $k'_F = k_F$, the $4f$ electrons remain localized and do not contribute to the Fermi volume. As discussed and also briefly mentioned in Chen *et al.* (2018b), if the Fermi surface of $CeCoIn_5$ expands from $k_F$ to $k'_F$ as the zero-temperature limit is approached, the band structure in the vicinity of $E_F$ should resemble that sketched in Fig. 4(a) and the spectral weight close to $k_F$ needs to vanish as $T \to 0$ so that the incoherent spectral weight at the Fermi energy is gapped out. The detection of such a, possibly very small, gap is challenging in view of the limited energy resolution and $k_z$ broadening effects of ARPES experiments as discussed in Sec. III. Note that, although it is expected that $k'_F \neq k_F$ in $CeCoIn_5$, results shown in Fig. 9(a) are indicative of a spectral weight increase near and at $k_F$ as the temperature is lowered from $T = 60$ to 17 K. Most likely, this is more than just a reflection of the limited energy resolution of the measurement, and instead indicates that the single-particle excitations are not of the Fermi liquid form depicted in Fig. 4(a). This is also corroborated by the strange metal behavior, encoded in an approximately linear-in-temperature dependence of the resistivity over a wide temperature window above the superconducting transition temperature ($T_c \sim 2.3$ K) (Petrovic, Pagliuso *et al.*, 2001). In Fig. 8, the temperature dependence of the resistivity $\rho$ of $CeCoIn_5$ is shown together with the magnetic resistivity, i.e., the difference between the resistivities of $CeCoIn_5$ and its nonmagnetic reference compound $LaCoIn_5$.

The ARPES study of Chen *et al.* (2017) also indicated the presence of $\omega/T$ scaling in the EDCs near the Γ point in an intermediate temperature range. This is reproduced in Fig. 9(c). Already at around 90 K, the EDCs multiplied by $T^{x_{\rm EDC}}$ (with $x_{\rm EDC} \approx 0.36$) collapse on a function depending only on $\omega/T$. This, however, should not be interpreted as reflecting an $\omega/T$ scaling of all single-particle excitations, which would imply a strict linear-in-$T$ behavior of the resistivity. Indeed, this scaling seems to be confined to the vicinity of the Γ point and is absent in the angle-integrated EDCs. Moreover, this peculiar scaling exists only in an intermediate $T$ range and fails below 20 K, as shown in Fig. 9(c). This conclusion appears to be compatible with the findings reported

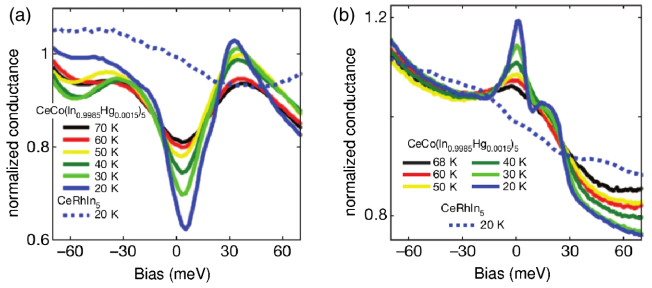


FIG. 10. Tunneling spectroscopy of $CeCoIn_5$ and $CeRhIn_5$: local conductance vs applied bias voltage for different temperatures on (a) Ce-terminated surfaces and (b) Co-(respectively, Rh-) terminated surfaces. The peak-dip-peak structure in conductance of $CeCoIn_5$ (a) is typical of a hybridization gap that is not obvious in $CeRhIn_5$, even at the lowest temperature. From (Aynajian *et al.*, 2012).

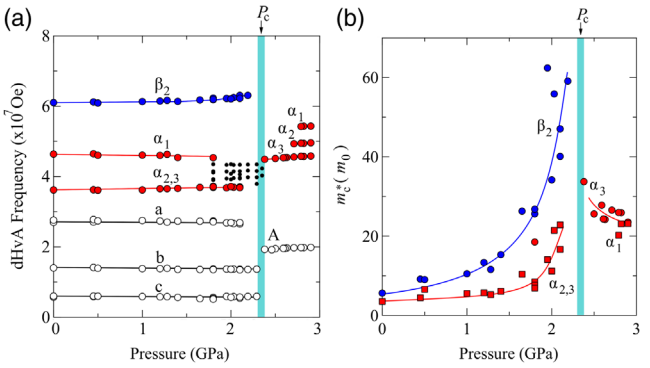


FIG. 11. de Haas–van Alphen measurements on $CeRhIn_5$. (a) Jump of the dHvA frequencies at $p_c$ indicating a reconstruction of the Fermi surface as the QCP is crossed. (b) Diverging effective mass upon approaching $p_c$ from above and below. From Shishido *et al.*, 2005.

by Aynajian *et al.* (2012), taking into account that tunneling into states with small lattice momenta is favored over tunneling into large-momentum states (Tersoff and Hamann, 1985; da Silva Neto *et al.*, 2013; Huang *et al.*, 2015). This demonstrates that ARPES and STM indeed provide information on the single-particle Green's function that can be directly compared to each other. It is, however, noteworthy that the temperature exponents accompanying this $\omega/T$ scaling in the intermediate temperature range from 20 to around 70 K differ somewhat depending on the measurement technique. While the STM-derived exponent is $x_{\mathrm{STM}} \approx 0.53$, the best fit of the ARPES data was obtained for $x_{\mathrm{EDC}} \approx 0.36$. The difference between the ARPES and STM results is most likely due to the dependence of the STM current on the degree of tunneling into $4f$ and $c$ electron states. This dependence is encoded in the Fano parameter.

STM studies on $CeCoIn_5$ (and to a much lesser extent on $CeRhIn_5$ and $CeIrIn_5$) have been performed by several groups (Ernst *et al.*, 2010; Aynajian *et al.*, 2012, 2014; Allan *et al.*, 2013; Zhou *et al.*, 2013; Haze *et al.*, 2018). In Figs. 10(a) and 10(b), results are shown for the local tunneling conductance of $CeCoIn_5$ very lightly doped with mercury (Hg) as well as $CeRhIn_5$ at different temperatures and on two different surfaces (Aynajian *et al.*, 2012). The Hg-doping induced disorder in $CeCoIn_5$ generates impurity scattering at the dopant sites which in turn can be systematically used to obtain lattice momentum-resolved information of the local DOS through QPI (Derry, Mitchell, and Logan, 2015). This use of QPI to extract the band structure near $E_F$ in the low-temperature limit, however, also has potential shortcomings that were already alluded to in Sec. III.

### C. $CeRhIn_5$

$CeRhIn_5$ is an antiferromagnet with a Néel temperature of $T_N = 3.8$ K at ambient pressure and has predominantly localized moments (Hegger *et al.*, 2000). Under pressure, $T_N$ can be suppressed to zero, thus tuning the system to a QCP at a critical pressure $p_c$. de Haas–van Alphen studies of $CeRhIn_5$ across the QCP display a clear jump of the dHvA frequencies at $p_c$, see Fig. 11(a), which implies that the Fermi surface changes discontinuously at the QCP (Shishido *et al.*, 2005). This compound therefore likely hosts a Kondo destruction QCP at $\delta_c = p_c$ ($\delta$ was defined in Sec. II). This conclusion is further corroborated by an effective mass that tends to diverge on approach to $p_c$; see Fig. 11(b). The latter reflects the vanishing of the wave-function renormalization factor $z$, depicted in Fig. 2(b), as the QCP is reached from either above or below $p_c$. In addition, transport measurements provide evidence for the Kondo destruction QCP (Park *et al.*, 2006, 2008). These low-energy quantum-critical features are accompanied by experiments measuring high-energy properties. The optical conductivity of $CeRhIn_5$ was reported by Mena, van der Marel, and Sarrao (2005) and shows the formation of a weak hybridization gap at high frequencies as temperature is lowered below the crossover scale $T_0$.

Despite evidence for the existence of a QCP featuring critical reconstruction of the Fermi surface in $CeRhIn_5$ under pressure, APRES and STM investigations of this compound are comparatively rare. This is largely due to difficulties in preparing a suitable surface and to the present impossibility of making these measurements under applied pressure. Early nonresonant ARPES investigations of $CeRhIn_5$ reported that the $4f$ electrons in this compound are predominantly itinerant (Moore *et al.*, 2002), whereas a second nonresonant ARPES study argued that the $4f$ electrons are nearly localized (Fujimori *et al.*, 2003).

Scanning tunneling spectroscopy data on Ce- and Rh-terminated surfaces of $CeRhIn_5$ show no clearly discernible Fano resonances, at least at around 20 K (Aynajian *et al.*, 2012); see Figs. 10(a) and 10(b). Interestingly, these results seem incompatible with high-resolution resonant ARPES data which point to the development of the $4f$-electron spectral weight near the Fermi energy, although the weight transfer is much weaker than in $CeCoIn_5$; see Fig. 12 (Chen *et al.*, 2018b). The spectral weight transfer depicted in Fig. 12 for the three bands crossing the Fermi surface also shows that, in the temperature range studied, spectral weight transfer occurs mainly near the $\gamma$ band crossing. The difference between the ARPES measurements of Chen *et al.* (2018b) and the STM investigation of Aynajian *et al.* (2012) is likely due to the increased surface sensitivity of STM. One possibility is that the Kondo temperature at the surface is reduced due to the reduced hybridization; a second is that the cleaving process to obtain suitable surfaces appears to be more problematic for

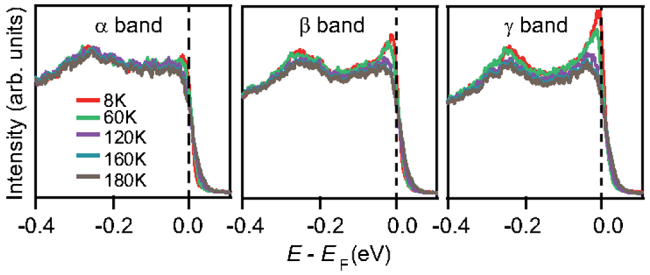


FIG. 12. EDCs of $CeRhIn_5$ vs temperature. The energy-distribution curves show the evolution of spectral weight with temperature near the Fermi energy $E_F$ for the three bands that cross $E_F$, labeled $\alpha$, $\beta$, and $\gamma$. Data were taken along the ΓM direction at $k_{\|} = -0.57$ Å$^{-1}$ ($\alpha$ band), $k_{\|} = -0.3$ Å$^{-1}$ ($\beta$ band), and $k_{\|} = -0.124$ Å$^{-1}$ ($\gamma$ band) and with an uncertainty of $\delta k_{\|} \sim 0.03$ Å$^{-1}$ for each of the three $k_{\|}$ values. From Chen *et al.*, 2018b.

$CeRhIn_5$ and $CeIrIn_5$ than for $CeCoIn_5$. In fact, recent STM results (Haze *et al.*, 2019) on epitaxially grown $CeRhIn_5$ with well-defined surfaces are very much in line with the ARPES measurements of Chen *et al.* (2018b). As in the case of the STM images of $YbRh_2Si_2$ [see Fig. 7(a)], these data are consistent with the dynamical Kondo effect taking place near the small Fermi surface.

### D. Further considerations

We now turn to several additional points that cut across specific Ce-115 families. First, the connection between the different Ce-115 families deserves further studies. As already discussed, isothermal dHvA measurements in $CeRhIn_5$ provide evidence for a sudden Fermi surface reconstruction at $p_c$. Intriguingly, frequencies of dominant $\alpha$ orbits at $p > p_c$ for $CeRhIn_5$ are very similar to those found for the large Fermi surface of $CeCoIn_5$ at atmospheric pressure (Shishido *et al.*, 2005). No Fermi surface reconstruction was found in $CeCoIn_5$. It is possible that a sudden Fermi surface reconstruction can still be found in $CeCoIn_5$ under a new tuning parameter, such as negative pressure. But it may also be that such an effect simply does not exist in $CeCoIn_5$, reflecting its inherent difference from $CeRhIn_5$. For example, the $4f - c$ hybridization is much larger in $CeCoIn_5$ than in $CeRhIn_5$, as evident in their STM spectra; see Fig. 10. As argued recently, this difference in overall hybridization can be traced to an anisotropic spatial extent of their $4f$ orbitals that is set by details of the crystal electric field wave function (Willers *et al.*, 2015; Sundermann *et al.*, 2019).

Second, an alternative explanation for the jump of the dHvA measurements across $p_c$ in $CeRhIn_5$ was proposed by Watanabe and Miyake (2010). It was suggested that the $4f$-valence fluctuations lead to a rapid valence change near $p_c$ and a strongly first order antiferromagnetic transition. The latter implies a large jump of the order parameter and, thus a large reconstruction of the Fermi surface. So far, however, all experimental evidence points to a continuous transition at $p_c$. In addition, canonical valence-fluctuating systems such as $CeSn_3$ ($CePd_3$) have specific-heat coefficients of 53 (37) mJ/(mol K$^2$), and effective Kondo temperatures of 770 (1120) K (Lawrence, Riseborough, and Parks, 1981). In those cases, the $4f$-occupancy $n_f$ will be far from 1 or 0 and, consequently, the entropy in the valence-fluctuation sector, which one can estimate by $R[n_f \ln n_f^{-1} + (1-n_f)\ln(1-n_f)^{-1}]$, will be a sizable fraction of $R \ln 2$. By contrast, in the quantum-critical regime of $CeRhIn_5$, the specific-heat coefficient is very large [$\gamma \approx 1.25$ J/(mol K$^2$)] (Park and Thompson, 2009), implying that $n_f$ is exceedingly close to 1. Thus, the valence-fluctuation sector will have a small entropy compared to the nearly $R \ln 2$ entropy in the spin sector and can hardly be the main driver of the critical fluctuations. In other words, the quantum criticality should primarily be driven by physics of the Kondo limit (Park *et al.*, 2006, 2008). Similar arguments apply to $CeCoIn_5$, $CeIrIn_5$, $YbRh_2Si_2$, and $CeCu_{5.9}Au_{0.1}$.

### E. Summary of Sec. V

We close this section by summarizing the status of ARPES and STM investigations in cerium-based 115 systems as discussed in this section.

By and large, the existing STM and ARPES results on the cerium-based 115 family are consistent with each other, given the requirements of surface quality and the associated difficulties. The recent high-resolution ARPES investigation of these 115 materials also shows that none of the three compounds follows the low-temperature band-structure expectations of a fully coherent heavy-electron Fermi liquid, encoded in Fig. 4(a). This is in line with other measurements, in particular, transport measurements, which suggest that none is in a Fermi liquid regime in the range where the ARPES measurements were made. Further, the limited energy resolution of state-of-the-art ARPES is still posing a major challenge in the heavy-electron materials class in which the associated energy scales are typically very small.

*High-energy features*: Existing ARPES and STM investigations of the 115 members show the initial onset of dynamical Kondo correlations around the $T_0$ temperature scale [Fig. 2(a)] and the concomitant onset of hybridization-gap formation. This is in line with optical conductivity measurements on these compounds (Chen and Wang, 2016). Comparing ARPES and STM data for the same compound gives complementary results that are compatible with each other and provide evidence for the existence of the hybridization-gap onset scale $T_0$.

*Low-energy features*: Neither in $CeCoIn_5$ nor in $CeRhIn_5$ has ARPES been able to confirm unambiguously the existence of either $k_F^L$ or $k_F^S$. While this may not be surprising due to the limited energy and momentum resolution currently available to ARPES, this finding is also compatible with the absence of Fermi liquid signatures in the investigated temperature range in these compounds; in this range, Fermi liquid signatures are absent as well in transport and thermodynamic properties. Isothermal measurements of dHvA have shown a sudden reconstruction of the Fermi surface across the pressure-induced QCP in $CeRhIn_5$, which provides strong evidence for a Kondo destruction QCP.

## VI. PROGRESS, CHALLENGES, AND PROSPECTS

### A. High-energy Kondo features

We have stressed that the initial onset of dynamical Kondo correlations or hybridization is expected, at the $T_0$ scale of

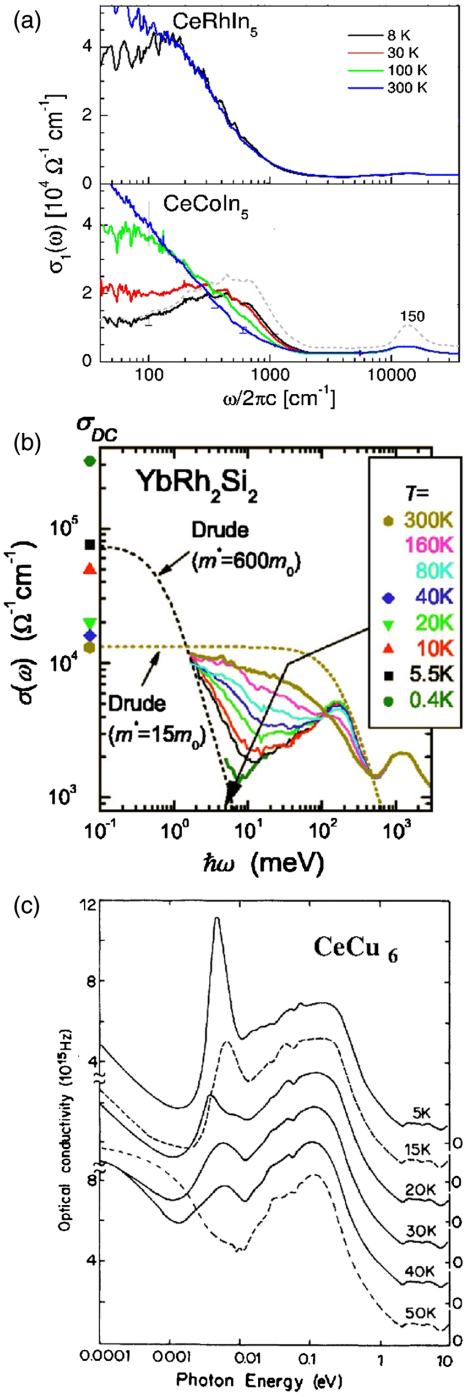


FIG. 13. Optical conductivity $\sigma(\omega, T)$ and evolution of the hybridization gap. (a) Although the hybridization gap in $CeRhIn_5$ (top) is overall less pronounced than that in the optical conductivity of $CeCoIn_5$ (bottom), the overall features for both compounds are in accordance with general expectations (see Fig. 3): at the highest measured $T$ a broad Drude peak exists out of which a hybridization gap develops below $\sqrt{T_0 D}$ as $T$ is lowered. From Mena, van der Marel, and Sarrao, 2005. (b) The hybridization gap in $YbRh_2Si_2$ evolves over a large $T$ region, starting well above 100 K. As the data are taken at zero external field, the system is located on the $\delta < \delta_c$ side (see Sec. II) and a Drude peak is therefore expected in $\sigma(\omega, T)$ at small $\omega$ and sufficiently low $T$. From Kimura *et al.*, 2006. (c) In $CeCu_6$ the optical conductivity develops a hybridization gap at around $\hbar\omega \approx 1$ meV below 50 K which is flanked toward higher energies by a pronounced peak. From Marabelli and Wachter, 1990.

Fig. 2, for all heavy-electron systems regardless of the nature of their ground states.

This scale is evident in $YbRh_2Si_2$ by STM and optical conductivity [Fig. 13(b)]. Similarly, the formation of a hybridization gap was manifested in $CeRhIn_5$ by optical conductivity measurements (Mena, van der Marel, and Sarrao, 2005), reproduced in Fig. 13(a), and, recently, by STM measurements (Haze *et al.*, 2019). Also for $CeCu_6$, which is near a QCP that is accessed by introducing Au substitution for Cu, a hybridization gap has been observed in the optical conductivity, see Fig. 13(c) (Marabelli and Wachter, 1990). This captures the high-energy $T_0$ scale for the onset of hybridization-gap formation [Fig. 2(a)] and indeed evolves smoothly across the critical substitution $x_c = 0.1$ based on photoemission measurements (Klein *et al.*, 2008). The $T_0$ scale is also evidenced by recent time-resolved measurements in the critical substitution range (Wetli *et al.*, 2018; Pal *et al.*, 2019). Here a terahertz irradiation pumps the system and disturbs the correlations between the local moments and conduction electrons. We can expect the underlying Kondo coupling to produce an initial echo at a time corresponding to $\hbar/k_B T_0$. Such a finite timescale is indeed observed both away from and at the QCP. Note that the Fermi liquid scale of $CeCu_6$ is 0.2 K (see Table I), which is not accessible by current experiments done at temperatures above 1.5 K. Nonetheless, it is conceivable that future experiments may probe not only the echo effect at $\hbar/k_B T_0$, but also the response in the scaling time regime much beyond $\hbar/k_B T_0$.

Table I compiles high-temperature and Fermi liquid energy scales of the heavy-electron compounds discussed in this Colloquium. This table lists both $T_0^{\rm hyb}$, the initial onset of the hybridization gap, and $T_0^{\rm en}$, based on the spin entropy $S$. These two high-energy scales can differ by as much as an order of magnitude, which is not too surprising given that the crossover of Kondo lattice systems from the high-temperature incoherent regime toward the low-temperature coherent, quantum critical, or ordered regime is rather broad. This crossover can be made even broader when the excited crystal field levels are involved. In practice, we propose to use

$$T_0 = \sqrt{T_0^{\rm hyb} T_0^{\rm en}} \tag{7}$$

as a measure of the crossover Kondo scale. Defined in this way, we can infer from Table I that $T_0$ is ~62 K in $YbRh_2Si_2$, ~50 K in $CeCoIn_5$, $\gtrsim$25 K in $CeRhIn_5$, and $\gtrsim$13 K in $CeCu_6$.

### B. Isothermal evolution at low temperatures

We discussed in Sec. II that, to assess the nature of quantum criticality (Kondo destruction versus SDW), the isothermal evolution of quasiparticle spectral weight at low temperatures is particularly informative. In $YbRh_2Si_2$, this was done through STM measurements as a function of magnetic field at $T = 0.3$ K, and the results (Seiro *et al.*, 2018) support the Kondo destruction scale that had been inferred from magnetotransport and thermodynamic measurements (Paschen *et al.*, 2004; Gegenwart *et al.*, 2007; Friedemann *et al.*, 2010). Further STM measurements at lower temperatures will clearly be instructive. Whether related STM studies can be carried out

in 115 systems is at the present time unclear, because the QCP is realized at a relatively large pressure ($CeRhIn_5$) or possibly at negative pressure ($CeCoIn_5$ and $CeIrIn_5$) (Sidorov *et al.*, 2002; Pham *et al.*, 2006). In these latter two cases, applying uniaxial tension might open the possibility of both ARPES and STM studies in a regime that would access their respective QCP. Similar isothermal studies by ARPES appear to be difficult, due to the low temperature that is needed, and also because ARPES cannot be performed in the presence of a magnetic field.

### C. Outlook

As previously discussed (see Sec. III), STM is a real space probe and thus generally lacks momentum resolution. It is, however, possible to extract information on the band structure near the Fermi energy using Friedel oscillations that occur near defects (Petersen *et al.*, 1998, 2000). Since STM is a surface probe, QPI provides only a projected band structure. Furthermore, the standard approach which is based on Born scattering is known to be insufficient in many cases (Toldin *et al.*, 2013). This limitation notwithstanding, it will be instructive to obtain band-structure information through Fourier transform STM on either side of the QCP to interpret QPI spectra in the quantum-critical fan of the QCP.

Critical Kondo destruction is accompanied by a particular kind of $\omega/T$ scaling. Recently, this type of scaling was demonstrated for the optical conductivity of $YbRh_2Si_2$ thin films grown by molecular beam epitaxy, studied by time-domain THz-transmisson spectroscopy (Prochaska *et al.*, 2020). This result would be surprising from the perspective of an SDW QCP, where only the spin dynamics is expected to be critical. However, it is in line with critical Kondo destruction (Prochaska *et al.*, 2020). Because the magnetic quantum phase transition is accompanied by the transition from a phase with asymptotically decoupled local-moment and conduction electron degrees of freedom to one in which the entangling of the two turns the $4f$ local moments into composite quasiparticles, it is natural that both the single-particle and charge dynamics are critical. Indeed, calculations at the Kondo destruction QCP in various large-$N$ limits (Zhu *et al.*, 2004; Kirchner *et al.*, 2005; Komijani and Coleman, 2019; Cai *et al.*, 2020) and, more recently, in the physical $N = 2$ case (Cai *et al.*, 2020) have shown such a singular charge dynamics. Intriguingly, this type of charge dynamical scaling in models of the Kondo limit smoothly connects to the $\omega/T$ scaling for the charge dynamics in the beyond-Landau-type quantum criticality in the mixed-valence regime (Pixley *et al.*, 2012).

Epitaxial thin films of members of the 115 family and $CeIn_3$ have been available for some time (Shishido *et al.*, 2010) but STM measurements on these films of $CeCoIn_5$ and $CeRhIn_5$ have been reported only very recently (Haze *et al.*, 2018, 2019). The observed onset of the hybridization gap in the STM spectrum demonstrates the high-energy $T_0$ scale which, as we have emphasized, is consistent with a Kondo destruction ground state in $CeRhIn_5$. It will be interesting to see whether a lattice mismatch between substrate and thin film might be used as a substitute for pressure tuning and to establish the range of $\omega/T$ scaling both within the general phase diagram and with respect to the type of correlator, i.e., single-particle excitations, two-particle correlators like the density-density, spin-spin, or current-current correlation functions, and their $n$-point ($n > 4$) counterparts.

We also briefly discussed in Sec. III that the underlying assumption in the interpretation of STM spectra in terms of the equilibrium local DOS is less justified at higher voltages. This may be particularly pertinent near the QCP, where the temperature of the measurement itself is expected to set the only relevant scale (Kirchner and Si, 2009). It would be interesting to explore the scaling of spectral density with bias voltage in the nonequilibrium regime which could be yet another way of unraveling the properties of the underlying QCP (Ribeiro, Zamani, and Kirchner, 2015; Zamani, Ribeiro, and Kirchner, 2016b).

We have so far focused on $YbRh_2Si_2$ and Ce-115 compounds. It will be instructive to carry out measurements of single-particle properties in other candidate heavy-electron materials for Kondo destruction (Stewart, 2001; Gegenwart, Si, and Steglich, 2008; Kirchner, Stockert, and Wirth, 2013; Si and Paschen, 2013). A case in point is CeNiAsO, a heavy-electron relative of the high-$T_c$ Fe-based oxypnictides. Here the recent neutron scattering experiments provide evidence for a local-moment antiferromagnetic order, whose ordering wave vector is determined by the RKKY interaction mediated by the conduction electron states near the small Fermi surface (i.e., the Fermi surface of the conduction electrons alone, with the $4f$ electrons localized) (Wu *et al.*, 2019), and transport measurements have suggested the possibility of a Kondo destruction QCP induced by either pressure or P-for-As doping (Luo *et al.*, 2014).

More broadly, there is the question of where to look for new examples of Kondo destruction criticality. If the $f - c$ hybridization is too strong, magnetic order would more likely be of the SDW type that, when tuned to $T = 0$, would result in a conventional QCP. Thus, weaker hybridization is expected to be a more favorable setting to access a possible Kondo destruction QCP. Alternatively, a low carrier density gives a small Fermi surface in a Kondo lattice and delays the full development of a Kondo singlet state with decreasing temperature. $CeNi_2As_{2-\delta}$ appears to be an example of such a case with evidence of Kondo destruction quantum criticality (Luo *et al.*, 2015). Finally, in the absence of tuning hybridization or carrier density, increasing frustration, whether through crystal structure or reduced dimensionality, offers an exciting opportunity for discovering new examples (Si, 2006; Fritsch *et al.*, 2014; Tokiwa *et al.*, 2015; Zhao *et al.*, 2019).

## VII. CONCLUSION

We have reviewed and compared recent ARPES and STM investigations on heavy-electron materials close to magnetic instabilities with a focus on Kondo destruction quantum criticality. Real-space and momentum-space spectroscopies combine the power of both methods (Nicoara *et al.*, 2006; Crepaldi *et al.*, 2013) which has proven to be useful in the study of complex materials such as the cuprate high-temperature superconductors (Markiewicz, 2004; Shen and Davis, 2008) and the Kondo insulator $SmB_6$ (Matt *et al.*, 2020). In the context of cerium- and ytterbium-based rare earth

intermetallics as well as actinide-based compounds, such a combination seems particularly promising given that much of the excitement and interest generated by these materials derives from the interplay of local and itinerant degrees of freedom. While Kondo screening is primarily a local phenomenon, a possible Fermi volume increase is best addressed in momentum space. Method-specific constraints, limited energy resolution, and the need for very low temperatures in order to resolve a Fermi momentum change across a Kondo destruction quantum-critical point pose unique challenges to both ARPES and STM investigations.

On the other hand, combining ARPES and STM results with other measurements, like resistivity and magnetotransport measurements, neutron scattering, and optical conductivity investigations, can provide a consistent picture of Kondo destruction quantum criticality that emerges as a function of some nonthermal tuning parameter and enables one to locate a specific compound in the general phase diagram of heavy-electron materials. This appears particularly relevant in the present context in order to aide a separation of bulk and surface contributions as both ARPES and STM are primarily surface sensitive. The change in symmetry and $c-f$ hybridization that typically occurs at surfaces can in Kondo systems substantially modify low-energy scales as compared to their bulk value.

We have emphasized the distinction between the spectroscopic properties that reflect the high-energy Kondo physics, such as the formation of the hybridization gap, and those that are capable of probing the nature of quantum criticality, such as low-temperature isothermal measurements across the quantum-critical point. The latter has become possible in the STM measurements of $YbRh_2Si_2$, which corroborates the Kondo destruction energy scale that had been extracted by isothermal magnetotransport and thermodynamic measurements. In $CeRhIn_5$, strong evidence for Kondo destruction in the one-electron excitation spectrum has been provided by quantum oscillation measurements across the critical pressure. It will certainly be instructive to explore further signatures of beyond-Landau quantum criticality in these and other heavy-electron systems.

## ACKNOWLEDGMENTS

We are grateful to the late Elihu Abrahams, Jim Allen, Pegor Aynajian, Ang Cai, Kai Grube, Nigel Hussey, Kevin Ingersent, Johann Kroha, Hilbert von Löhneysen, Yuji Matsuda, Emilian Nica, Jed H. Pixley, Pedro Ribeiro, Rong Yu, Zuo-Dong Yu, Farzaneh Zamani, and Gertrud Zwicknagl for useful discussions. Part of these discussions took place at the 2018 Hangzhou Workshop on Quantum Matter and we thank all participants of the workshop. This work was in part supported by the National Key R&D Program of the MOST of China, Grant No. 2016YFA0300200 (S. K., Q. C., and D. F.), the National Science Foundation of China, No. 11774307 (S. K.), and No. 11874330 (Q. C.), and the Science Challenge Project, Grant No. TZ2016004 (D. F.). The work in Vienna was supported by the FWF (Project No. P 29296-N27) and the European Microkelvin Platform (H2020 Project No. 824109). The work at Los Alamos was performed under the auspices of the U.S. Department of Energy, Division of Materials Sciences and Engineering. The work at Rice was in part supported by the NSF (DMR-1920740) and the Robert A. Welch Foundation (C-1411). S. K. acknowledges support by MOST of Taiwan, Grant No. 108-2811-M-009-500 and the hospitality of NCTU, Hsinchu. Donglai Feng is supported by the Anhui Initiative in Quantum Information Technologies. Q. S. acknowledges the hospitality and the support by a Ulam Scholarship from the Center for Nonlinear Studies at Los Alamos National Laboratory and the hospitality of the Aspen Center for Physics (NSF, PHY-1607611).

## REFERENCES

Allan, M. P., F. Massee, D. K. Morr, J. V. Dyke, A. W. Rost, A. P. Mackenzie, C. Petrovic, and J. C. Davis, 2013, Nat. Phys. **9**, 468.

Amato, A., D. Jaccard, J. Flouquet, F. Lapierre, J. L. Tholence, R. A. Fisher, S. E. Lacy, J. A. Olsen, and N. E. Phillips, 1987, J. Low Temp. Phys. **68**, 371.

Aronson, M. C., R. Osborn, R. A. Robinson, J. W. Lynn, R. Chau, C. L. Seaman, and M. B. Maple, 1995, Phys. Rev. Lett. **75**, 725.

Aynajian, P., E. H. da Silva Neto, A. Gyenis, R. E. Baumbach, J. D. Thompson, Z. Fisk, E. D. Bauer, and A. Yazdani, 2012, Nature (London) **486**, 201.

Aynajian, P., E. H. da Silva Neto, C. V. Parkera, Y. Huangb, A. Pasupathy, J. Mydosh, and A. Yazdani, 2010, Proc. Natl. Acad. Sci. U.S.A. **107**, 10383.

Aynajian, P., E. H. da Silva Neto, B. B. Zhou, S. Misra, R. E. Baumbach, Z. Fisk, J. Mydosh, J. D. Thompson, E. D. Bauer, and A. Yazdani, 2014, J. Phys. Soc. Jpn. **83**, 061008.

Bachmann, M. D., *et al.*, 2019, Science **366**, 221.

Bardeen, J., 1961, Phys. Rev. Lett. **6**, 57.

Benlagra, A., T. Pruschke, and M. Vojta, 2011, Phys. Rev. B **84**, 195141.

Betbeder-Matibet, O., and P. Nozières, 1966, Ann. Phys. (N.Y.) **37**, 17.

Burch, K. S., S. V. Dordevic, F. P. Mena, A. B. Kuzmenko, D. van der Marel, J. L. Sarrao, J. R. Jeffries, E. D. Bauer, M. B. Maple, and D. N. Basov, 2007, Phys. Rev. B **75**, 054523.

Cai, A., H. Hu, K. Ingersent, S. Paschen, and Q. Si, 2019, "Dynamical Kondo effect and Kondo destruction in effective models for quantum-critical heavy fermion metals," arXiv:1904.11471.

Cai, A., Z. Yu, H. Hu, S. Kirchner, and Q. Si, 2020, Phys. Rev. Lett. **124**, 027205.

Chen, Q. Y., *et al.*, 2017, Phys. Rev. B **96**, 045107.

Chen, Q. Y., *et al.*, 2018a, Phys. Rev. B **97**, 075149.

Chen, Q. Y., *et al.*, 2018b, Phys. Rev. Lett. **120**, 066403.

Chen, R. Y., and N. L. Wang, 2016, Rep. Prog. Phys. **79**, 064502.

Chen, Y., W. B. Jiang, C. Y. Guo, F. Ronning, E. D. Bauer, T. Park, H. Q. Yuan, Z. Fisk, J. D. Thompson, and X. Lu, 2015, Phys. Rev. Lett. **114**, 146403.

Coleman, P., C. Pépin, Q. Si, and R. Ramazashvili, 2001, J. Phys. Condens. Matter **13**, R723.

Coleman, P., and A. J. Schofield, 2005, Nature (London) **433**, 226.

Cornut, B., and B. Coqblin, 1972, Phys. Rev. B **5**, 4541.

Costi, T. A., and N. Manini, 2002, J. Low Temp. Phys. **126**, 835.

Crepaldi, A., S. Pons, E. Frantzeskakis, F. Calleja, M. Etzkorn, A. P. Seitsonen, K. Kern, H. Brune, and M. Grioni, 2013, Phys. Rev. B **87**, 115138.

Custers, J., P. Gegenwart, H. Wilhelm, K. Neumaier, Y. Tokiwa, O. Trovarelli, C. Geibel, F. Steglich, C. Pépin, and P. Coleman, 2003, Nature (London) **424**, 524.

da Silva Neto, E. H., P. Aynajian, R. E. Baumbach, E. D. Bauer, J. Mydosh, S. Ono, and A. Yazdani, 2013, Phys. Rev. B **87**, 161117.
Derry, P. G., A. K. Mitchell, and D. E. Logan, 2015, Phys. Rev. B **92**, 035126.
Doniach, S., 1977, Physica B+C (Amsterdam) **91**, 231.
Ernst, S., S. Kirchner, C. Krellner, C. Geibel, G. Zwicknagl, F. Steglich, and S. Wirth, 2011, Nature (London) **474**, 362.
Ernst, S., S. Wirth, F. Steglich, Z. Fisk, J. L. Sarrao, and J. D. Thompson, 2010, Phys. Status Solidi B **247**, 624.
Fano, U., 1961, Phys. Rev. **124**, 1866.
Figgins, J., and D. K. Morr, 2010, Phys. Rev. Lett. **104**, 187202.
Fischer, H. E., E. T. Swartz, R. O. Pohl, B. A. Jones, J. W. Wilkins, and Z. Fisk, 1987, Phys. Rev. B **36**, 5330.
Fisk, Z., J. L. Smith, H. R. Ott, and B. Batlogg, 1985, J. Magn. Magn. Mater. **52**, 79.
Friedemann, S., N. Oeschler, C. Krellner, C. Geibel, F. Steglich, S. Paschen, S. Kirchner, and Q. Si, 2010, Proc. Natl. Acad. Sci. U.S.A. **107**, 14547.
Fritsch, V., N. Bagrets, G. Goll, W. Kittler, M. J. Wolf, K. Grube, C.-L. Huang, and H. v. Löhneysen, 2014, Phys. Rev. B **89**, 054416.
Fujimori, S.-i., T. Okane, J.Okamoto, K. Mamiya, and Y. Muramatsu, 2003, Phys. Rev. B **67**, 144507.
Fujimori, S.-i., *et al.*, 2006, Phys. Rev. B **73**, 224517.
Gegenwart, P., J. Custers, C. Geibel, K. Neumaier, T. Tayama, K. Tenya, O. Trovarelli, and F. Steglich, 2002, Phys. Rev. Lett. **89**, 056402.
Gegenwart, P., Q. Si, and F. Steglich, 2008, Nat. Phys. **4**, 186.
Gegenwart, P., Y. Tokiwa, T. Westerkamp, F. Weickert, J. Custers, J. Ferstl, C. Krellner, C. Geibel, P. Kerschl, K.-H. Müller, and F. Steglich, 2006, New J. Phys. **8**, 171.
Gegenwart, P., T. Westerkamp, C. Krellner, Y. Tokiwa, S. Paschen, C. Geibel, F. Steglich, E. Abrahams, and Q. Si, 2007, Science **315**, 969.
Glossop, M., and K. Ingersent, 2007, Phys. Rev. Lett. **99**, 227203.
Grempel, D. R., and Q. Si, 2003, Phys. Rev. Lett. **91**, 026401.
Grube, K., S. Zaum, O. Stockert, Q. Si, and H. v. Löhneysen, 2017, Nat. Phys. **13**, 742.
Haule, K., C.-H. Yee, and K. Kim, 2010, Phys. Rev. B **81**, 195107.
Haze, M., R. Peters, Y. Torii, T. Suematsu, D. S. M. Naritsuka, Y. Kasahara, T. Shibauchi, T. Terashima, and Y. Matsuda, 2019, J. Phys. Soc. Jpn. **88**, 014706.
Haze, M., Y. Torii, R. Peters, S. Kasahara, Y. Kasahara, T. Shibauchi, T. Terashima, and Y. Matsuda, 2018, J. Phys. Soc. Jpn. **87**, 034702.
Hegger, H., C. Petrovic, E. G. Moshopoulou, M. F. Hundley, J. L. Sarrao, Z. Fisk, and J. D. Thompson, 2000, Phys. Rev. Lett. **84**, 4986.
Hertz, J., 1976, Phys. Rev. B **14**, 1165.
Hewson, A. C., 1993, *The Kondo Problem to Heavy Fermions* (Cambridge University Press, Cambridge, England).
Huang, D., C.-L. Song, T. A. Webb, S. Fang, C.-Z. Chang, J. S. Moodera, E. Kaxiras, and J. E. Hoffman, 2015, Phys. Rev. Lett. **115**, 017002.
Hüfner, S., 2003, *Photoelectron Spectroscopy* (Springer-Verlag, Berlin/Heidelberg).
Jang, S., J. D. Denlinger, J. W. Allen, V. S. Zapf, M. B. Maple, J. N. Kim, B. G. Jang, and J. H. Shim, 2017, "Evolution of the Kondo lattice electronic structure above the transport coherence temperature," arXiv:1704.08247.
Khodas, M., and A. M. Finkel'stein, 2003, Phys. Rev. B **68**, 155114.
Kimura, S., J. Sichelschmidt, J. Ferstl, C. Krellner, C. Geibel, and F. Steglich, 2006, Phys. Rev. B **74**, 132408.
Kirchner, S., and Q. Si, 2009, Phys. Rev. Lett. **103**, 206401.
Kirchner, S., O. Stockert, and S. Wirth, 2013, Phys. Status Solidi B **250**, 424.
Kirchner, S., L. Zhu, Q. Si, and D. Natelson, 2005, Proc. Natl. Acad. Sci. U.S.A. **102**, 18824.
Klein, M., A. Nuber, F. Reinert, J. Kroha, O. Stockert, and H. v. Löhneysen, 2008, Phys. Rev. Lett. **101**, 266404.
Kohno, H., and K. Yamada, 1988, Prog. Theor. Phys. **80**, 623.
Koitzsch, A., T. K. Kim, U. Treske, M. Knupfer, B. Büchner, M. Richter, I. Opahle, R. Follath, E. D. Bauer, and J. L. Sarrao, 2013, Phys. Rev. B **88**, 035124.
Koitzsch, A., *et al.*, 2008, Phys. Rev. B **77**, 155128.
Koitzsch, A., *et al.*, 2009, Phys. Rev. B **79**, 075104.
Komijani, Y., and P. Coleman, 2019, Phys. Rev. Lett. **122**, 217001.
Kroha, J., S. Kirchner, G. Sellier, P. Wölfle, D. Ehm, F. Reinert, S. Hüfner, and C. Geibel, 2003, Physica E (Amsterdam) **18**, 69.
Kummer, K., *et al.*, 2015, Phys. Rev. X **5**, 011028.
Lawrence, J. M., P. S. Riseborough, and R. D. Parks, 1981, Rep. Prog. Phys. **44**, 1.
Lawrence, J. M., C. H. Wang, A. D. Christianson, and E. D. Bauer, 2011, J. Phys. Condens. Matter **23**, 094210.
Löhneysen, H. v., T. Pietrus, G. Portisch, H. G. Schlager, A. Schröder, M. Sieck, and T. Trappmann, 1994, Phys. Rev. Lett. **72**, 3262.
Löhneysen, H. v., A. Rosch, M. Vojta, and P. Wölfle, 2007, Rev. Mod. Phys. **79**, 1015.
Luo, Y., F. Ronning, N. Wakeham, X. Lu, T. Park, Z.-A. Xu, and J. D. Thompson, 2015 Proc. Natl. Acad. Sci. U.S.A. **112**, 13520.
Luo, Y., *et al.*, 2014, Nat. Mater. **13**, 777.
Maltseva, M., M. Dzero, and P. Coleman, 2009, Phys. Rev. Lett. **103**, 206402.
Marabelli, F., and P. Wachter, 1990, Phys. Rev. B **42**, 3307.
Markiewicz, R. S., 2004, Phys. Rev. B **69**, 214517.
Matt, C. E., *et al.*, 2020, "Consistency between ARPES and STM measurements on $SmB_6$," arXiv:1810.13442 Phys. Rev. B (to be published).
Mena, F. P., D. van der Marel, and J. L. Sarrao, 2005, Phys. Rev. B **72**, 045119.
Millis, A. J., 1993, Phys. Rev. B **48**, 7183.
Mo, S.-K., *et al.*, 2012, Phys. Rev. B **85**, 241103(R).
Moore, D. P., T. Durakiewicz, J. J. Joyce, A. J. Arko, L. A. Moralesa, J. L. Sarrao, P. G. Pagliuso, J. M. Wills, and C. G. Olson, 2002, Physica B (Amsterdam) **312-313**, 134.
Moriya, T., 1985, *Spin Fluctuations in Itinerant Electron Magnetism* (Springer, Berlin).
Movshovich, R., M. Jaime, J. D. Thompson, C. Petrovic, Z. Fisk, P. G. Pagliuso, and J. L. Sarrao, 2001, Phys. Rev. Lett. **86**, 5152.
Nicoara, N., E. Román, J. M. Gómez-Rodriguez, J. A. Martin-Gago, and J. Méndez, 2006, Org. Electron. **7**, 287.
Paglione, J., T. A. Sayles, P.-C. Ho, J. R. Jeffries, and M. B. Maple, 2007, Nat. Phys. **3**, 703.
Pal, S., C. Wetli, F. Zamani, O. Stockert, H. v. Löhneysen, M. Fiebig, and J. Kroha, 2019, Phys. Rev. Lett. **122**, 096401.
Park, T., F. Ronning, H. Q. Yuan, M. B. Salamon, R. Movshovich, J. L. Sarrao, and J. D. Thompson, 2006, Nature (London) **440**, 65.
Park, T., V. A. Sidorov, F. Ronning, J.-X. Zhu, Y. Tokiwa, H. Lee, E. D. Bauer, R. Movshovich, J. L. Sarrao, and J. D. Thompson, 2008, Nature (London) **456**, 366.
Park, T., and J. D. Thompson, 2009, New J. Phys. **11**, 055062.
Paschen, S., S. Friedemann, S. Wirth, F. Steglich, S. Kirchner, and Q. Si, 2016, J. Magn. Magn. Mater. **400**, 17.
Paschen, S., T. Lühmann, S. Wirth, P. Gegenwart, O. Trovarelli, C. Geibel, F. Steglich, P. Coleman, and Q. Si, 2004, Nature (London) **432**, 881.
Pépin, C., 2007, Phys. Rev. Lett. **98**, 206401.
Petersen, L., P. Hofmann, E. Plummer, and F. Besenbacher, 2000, J. Electron Spectrosc. Relat. Phenom. **109**, 97.

Petersen, L., P. T. Sprunger, P. Hofmann, E. Lægsgaard, B. G. Briner, M. Doering, H.-P. Rust, A. M. Bradshaw, F. Besenbacher, and E. W. Plummer, 1998, Phys. Rev. B **57**, R6858.
Petrovic, C., R. Movshovich, M. Jaime, P. G. Pagliuso, M. F. Hundley, J. L. Sarrao, Z. Fisk, and J. D. Thompson, 2001, Europhys. Lett. **53**, 354.
Petrovic, C., P. G. Pagliuso, M. F. Hundley, R. Movshovich, J. L. Sarrao, J. D. Thompson, Z. Fisk, and P. Monthoux, 2001, J. Phys. Condens. Matter **13**, L337.
Pfau, H., *et al.*, 2012, Nature (London) **484**, 493.
Pham, L. D., T. Park, S. Maquilon, J. D. Thompson, and Z. Fisk, 2006, Phys. Rev. Lett. **97**, 056404.
Pixley, J. H., S. Kirchner, K. Ingersent, and Q. Si, 2012, Phys. Rev. Lett. **109**, 086403.
Plihal, M., and J. W. Gradzuk, 2001, Phys. Rev. B **63**, 085404.
Poudel, L., J. M. Lawrence, L. S. Wu, G. Ehlers, Y. Qiu, A. F. May, F. Ronning, M. D. Lumsden, D. Mandrus, and A. D. Christianson, 2019, npj Quantum Mater. **4**, 52.
Prochaska, L., *et al.*, 2020, Science **367**, 285.
Reinert, F., D. Ehm, S. Schmidt, G. Nicolay, S. Hüfner, J. Kroha, O. Trovarelli, and C. Geibel, 2001, Phys. Rev. Lett. **87**, 106401.
Ribeiro, P., F. Zamani, and S. Kirchner, 2015, Phys. Rev. Lett. **115**, 220602.
Ronning, F., C. Capan, A. Bianchi, R. Movshovich, A. Lacerda, M. F. Hundley, J. D. Thompson, P. G. Pagliuso, and J. L. Sarrao, 2005, Phys. Rev. B **71**, 104528.
Sachdev, S., 1999, *Quantum Phase Transitions* (Cambridge University Press, Cambridge, England).
Schiller, A., and S. Hershfield, 2000, Phys. Rev. B **61**, 9036.
Schmidt, A. R., M. H. Hamidian, P. Wahl, F. Meier, A. V. Balatsky, J. D. Garrett, T. J. Williams, G. M. Luke, and J. C. Davis, 2010, Nature (London) **465**, 570.
Schrieffer, J. R., and P. A. Wolff, 1966, Phys. Rev. **149**, 491.
Schröder, A., G. Aeppli, E. Bucher, R. Ramazashvili, and P. Coleman, 1998, Phys. Rev. Lett. **80**, 5623.
Schröder, A., G. Aeppli, R. Coldea, M. Adams, O. Stockert, H. v. Löhneysen, E. Bucher, R. Ramazashvili, and P. Coleman, 2000, Nature (London) **407**, 351.
Seiro, S., L. Jiao, S. Kirchner, S. Hartmann, S. Friedemann, C. Krellner, C. Geibel, Q. Si, F. Steglich, and S. Wirth, 2018, Nat. Commun. **9**, 3324.
Senthil, T., M. Vojta, and S. Sachdev, 2004, Phys. Rev. B **69**, 035111.
Settai, R., H. Shishido, S. Ikeda, Y. Murakawa, M. Nakashima, D. Aoki, Y. Haga, H. Harima, and Y. Onuki, 2001, J. Phys. Condens. Matter **13**, L627.
Shen, K. M., and J. S. Davis, 2008, Mater. Today **11**, 14.
Shishido, H., R. Settai, H. Harima, and Y. Ōnuki, 2005, J. Phys. Soc. Jpn. **74**, 1103.
Shishido, H., T. Shibauchi, K. Yasu, T. Kato, H. Kontani, T. Terashima, and Y. Matsuda, 2010, Science **327**, 980.
Shishido, H., *et al.*, 2002, J. Phys. Soc. Jpn. **71**, 162.
Si, Q., 2006, Physica B (Amsterdam) **378-380**, 23.
Si, Q., and S. Paschen, 2013, Phys. Status Solidi B **250**, 425.
Si, Q., J. H. Pixley, E. Nica, S. J. Yamamoto, P. Goswami, R. Yu, and S. Kirchner, 2014, J. Phys. Soc. Jpn. **83**, 061005.
Si, Q., S. Rabello, K. Ingersent, and J. Smith, 2001, Nature (London) **413**, 804.
Si, Q., and F. Steglich, 2010, Science **329**, 1161.
Si, Q., J.-X. Zhu, and D. R. Grempel, 2005, J. Phys. Condens. Matter **17**, R1025.
Sidorov, V. A., M. Nicklas, P. G. Pagliuso, J. L. Sarrao, Y. Bang, A. V. Balatsky, and J. D. Thompson, 2002, Phys. Rev. Lett. **89**, 157004.
Singh, S., C. Capan, M. Nicklas, M. Rams, A. Gladun, H. Lee, J. F. DiTusa, Z. Fisk, F. Steglich, and S. Wirth, 2007, Phys. Rev. Lett. **98**, 057001.
Singley, E. J., D. N. Basov, E. D. Bauer, and M. B. Maple, 2002, Phys. Rev. B **65**, 161101(R).
Stewart, G. R., 2001, Rev. Mod. Phys. **73**, 797.
Stockert, O., S. Kirchner, F. Steglich, and Q. Si, 2012, J. Phys. Soc. Jpn. **81**, 011001.
Strocov, V., 2003, J. Electron Spectrosc. Relat. Phenom. **130**, 65.
Sundermann, M., *et al.*, 2019, Phys. Rev. B **99**, 235143.
Taupin, M., G. Knebel, T. D. Matsuda, G. Lapertot, Y. Machida, K. Izawa, J.-P. Brison, and J. Flouquet, 2015, Phys. Rev. Lett. **115**, 046402.
Tersoff, J., and D. R. Hamann, 1985, Phys. Rev. B **31**, 805.
Thompson, J. D., and Z. Fisk, 2012, J. Phys. Soc. Jpn. **81**, 011002.
Tokiwa, Y., C. Stingl, M.-S. Kim, T. Takabatake, and P. Gegenwart, 2015, Sci. Adv. **1**, e1500001.
Toldin, F. P., J. Figgins, S. Kirchner, and D. K. Morr, 2013, Phys. Rev. B **88**, 081101(R).
Trovarelli, O., C. Geibel, S. Mederle, C. Langhammer, F. M. Grosche, P. Gegenwart, M. Lang, G. Sparn, and F. Steglich, 2000, Phys. Rev. Lett. **85**, 626.
Tsujii, N., H. Kontani, and K. Yoshimura, 2005, Phys. Rev. Lett. **94**, 057201.
Újsághy, O., J. Kroha, L. Szunyogh, and A. Zawadowski, 2000, Phys. Rev. Lett. **85**, 2557.
Wadati, H., T. Yoshida, A. Chikamatsu, H. Kumigashira, M. Oshima, H. Eisaki, Z.-X. Shen, T. Mizokawa, and A. Fujimori, 2006, Phase Transitions **79**, 617.
Watanabe, S., and K. Miyake, 2010, J. Phys. Soc. Jpn. **79**, 033707.
Wetli, C., S. Pal, J. Kroha, K. Kliemt, C. Krellner, O. Stockert, H. v. Löhneysen, and M. Fiebig, 2018, Nat. Phys. **14**, 1103.
Willers, T., *et al.*, 2015, Proc. Natl. Acad. Sci. U.S.A. **112**, 2384.
Wirth, S., Y. Prots, M. Wedel, S. Ernst, S. Kirchner, Z. Fisk, J. D. Thompson, F. Steglich, and Y. Grin, 2014, J. Phys. Soc. Jpn. **83**, 061009.
Wölfle, P., Y. Dubi, and A. V. Balatsky, 2010, Phys. Rev. Lett. **105**, 246401.
Wu, S., *et al.*, 2019, Phys. Rev. Lett. **122**, 197203.
Yazdani, A., E. H. da Silva Neto, and P. Aynajian, 2016, Annu. Rev. Condens. Matter Phys. **7**, 11.
Zamani, F., P. Ribeiro, and S. Kirchner, 2016a, New J. Phys. **18**, 063024.
Zamani, F., P. Ribeiro, and S. Kirchner, 2016b, J. Magn. Magn. Mater. **400**, 7.
Zaum, S., K. Grube, R. Schäfer, E. D. Bauer, J. D. Thompson, and H. v. Löhneysen, 2011, Phys. Rev. Lett. **106**, 087003.
Zhao, H., *et al.*, 2019, Nat. Phys. **15**, 1261.
Zhou, B. B., S. Misra, E. H. da Silva Neto, P. Aynajian, R. E. Baumbach, J. D. Thompson, E. D. Bauer, and A. Yazdani, 2013, Nat. Phys. **9**, 474.
Zhu, J.-X., D. R. Grempel, and Q. Si, 2003, Phys. Rev. Lett. **91**, 156404.
Zhu, J.-X., S. Kirchner, R. Bulla, and Q. Si, 2007, Phys. Rev. Lett. **99**, 227204.
Zhu, L., S. Kirchner, Q. Si, and A. Georges, 2004, Phys. Rev. Lett. **93**, 267201.